THE ASTROPHYSICAL JOURNAL, 559:754–784, 2001 October 1

THE METAMORPHOSIS OF TIDALLY STIRRED DWARF GALAXIES

LUCIO MAYER,[1] FABIO GOVERNATO,[2] MONICA COLPI,[3] BEN MOORE,[4] THOMAS QUINN,[1] JAMES WADSLEY,[5] JOACHIM STADEL,[1,6] AND GEORGE LAKE[1]

Received 2001 March 26; accepted 2001 June 5

ABSTRACT

We present results from high-resolution N-body/SPH (smoothed particle hydrodynamic) simulations of rotationally supported dwarf irregular galaxies moving on bound orbits in the massive dark matter halo of the Milky Way. The dwarf models span a range in disk surface density and the masses and sizes of their dark halos are consistent with the predictions of cold dark matter cosmogonies. We show that the strong tidal field of the Milky Way determines severe mass loss in their halos and disks and induces bar and bending instabilities that transform low surface brightness dwarfs (LSBs) into dwarf spheroidals (dSphs) and high surface brightness dwarfs (HSBs) into dwarf ellipticals (dEs) in less than 10 Gyr. The final central velocity dispersions of the remnants are in the range 8–30 km s^{-1} and their final v/σ falls to values less than 0.5, matching well the kinematics of early-type dwarfs. The transformation requires the orbital time of the dwarf to be $\lesssim$3–4 Gyr, which implies a halo as massive and extended as predicted by hierarchical models of galaxy formation to explain the origin of even the farthest dSph satellites of the Milky Way, Leo I, and Leo II. We show that only dwarfs with central dark matter densities as high as those of Draco and Ursa Minor can survive for 10 Gyr in the proximity of the Milky Way. A correlation between the central density and the distance of the dwarfs from the primary galaxy is indeed expected in hierarchical models, in which the densest objects should have small orbital times because of their early formation epochs. Part of the gas is stripped and part is funneled to the center because of the bar, generating one strong burst of star formation in HSBs and smaller, multiple bursts in LSBs. Therefore, the large variety of star formation histories observed in Local Group dSphs arises because different types of dIrr progenitors respond differently to the external perturbation of the Milky Way. Our evolutionary model naturally explains the morphology-density relation observed in the Local Group and in other nearby loose groups. Extended low surface brightness stellar and gaseous streams originate from LSBs and follow the orbit of the dwarfs for several gigayears. Because of their high velocities, unbound stars projected along the line of sight can lead to overestimating the mass-to-light ratio of the bound remnant by a factor $\lesssim$2, but this does not eliminate the need of extremely high dark matter contents in some of the dSphs.

Subject headings: galaxies: dwarf — galaxies: evolution — galaxies: interactions — galaxies: kinematics and dynamics — Local Group — methods: n-body simulations

1. INTRODUCTION

Since the fundamental review by Paul Hodge in 1971, the total dwarf population of the Local Group has more than doubled. The current census of dwarf galaxies, faint objects with luminosities $-18 < M_B < -9$, is around 40, including all objects that lie within or very close to the zero-velocity surface of the Local Group (Mateo 1998; van den Bergh 1999). These tiny galaxies are either dwarf irregulars (dIrrs), dwarf ellipticals (dEs), or dwarf spheroidals (dSphs) (Grebel 1999; van den Bergh 1999). Dwarf irregulars ($M_B \leq -11$) are irregularly shaped galaxies with recent or ongoing star formation and generally quite low surface brightness ($\mu_B \sim$ 23 mag arcsec^{-2}). The dEs have ellipsoidal shapes, are fairly luminous ($-17 < M_B < -15$), and typically have a central surface brightness ($\mu_B \leq 21$ mag arcsec^{-2}) higher than that of bright dIrrs such as the LMC or IC 10 (Mateo 1998). Similar to their counterparts found in galaxy clusters (Ferguson & Binggeli 1994; James 1991), some of them have blue nuclei (Bica, Alloin, & Schmidt 1990; Jones et al. 1996). They contain mainly old (>10 Gyr) and intermediate-age (1–10 Gyr) stellar populations and show, in part, recent star formation. The dSphs number some of the least luminous ($M_B \sim -9$) and lowest surface brightness galaxies known to date ($\mu_B \geq 24$ mag arcsec^{-2}). They do not have nuclei or significant central concentrations and are dominated by old or intermediate-age stellar populations. Star formation in some of them has ceased a few Gyr ago, while in others it has been more extended in time and episodic (Hurley-Keller, Mateo, & Nemec 1998; Grebel 1999). A few galaxies have properties intermediate between dIrrs and dSphs and may be evolving from dIrrs to dSphs (Grebel 1999). A clear progression from dIrrs to dSphs is evident in their H I-to-total baryonic mass (stars + gas): this ranges between 7% and 50% for dIrrs, it is between 1% and 10% in transition systems, while it is lower than 0.1% in dSphs and dEs.

The Local Group dwarf galaxies show a striking morphology-density relation (Grebel 1999) which seems to be featured even in other nearby loose groups (Karachentsev et al. 2000): dIrrs are found far away from either the Milky Way or M31, while dSphs and dEs lie

[1] Department of Astronomy, Physics/Astronomy Building, University of Washington, Stevens Way, Box 351580, Seattle, WA 98195-1580; mayer@astro.washington.edu, trq@astro.washington.edu, stadel@astro.washington.edu, lake@astro.washington.edu.

[2] Osservatorio Astronomico di Brera, Via Bianchi 46, Merate (LC), I-23807 Italy; fabio@merate.mi.astro.it.

[3] Dipartimento di Fisica, Università degli Studi di Milano-Bicocca, P. della Scienza 3, Milano, I-20126 Italy; Monica.Colpi@mib.infn.it.

[4] Department of Astronomy, University of Durham, Durham, UK; Ben.Moore@durham.ac.uk.

[5] Department of Physics and Astronomy, McMaster University, Hamilton, Ontario L8S 4M1, Canada; wadsley@physics.mcmaster.ca.

[6] Department of Physics and Astronomy, University of Victoria, Elliot Building, 3800 Finnerty Road, Victoria, BC V8P 1A1, Canada.

within 300–400 kpc from the center of the primary galaxies. The distances of dSphs are sufficiently small to postulate that they are satellites of the dominant spirals, moving on bound orbits in their large dark matter halos (Peebles et al. 1989).

Kinematical analysis of dwarf galaxies in the Local Group highlights an important distinction between dSphs and dIrrs, namely, *their different angular momentum content*. The stars in dSphs and dEs are supported by velocity dispersion (typically $v/\sigma < 0.5$, see Mateo 1998 and Bender, Burstein, & Faber 1992), while the neutral hydrogen is known to rotate in nearly all dIrrs ($v/\sigma > 1$). The kinematics of the stellar component is still not available for dIrrs but equilibrium arguments suggest that the stars should be arranged in a rotating disk component as the gas. Only the faintest Local Group dIrrs, such as Sag DIG and GR 8 ($M_B > -12$), are dominated by rotation inside their half-light radius but are pressure supported at large radii (Carignan, Beaulieu, & Freeman 1990; Hoffman et al. 1996; Lo, Sargent, & Young 1993).

Despite these differences, the surface brightness profiles of dIrrs and dSphs are quite similar. Traditionally, fits with exponential profiles are preferred for dIrrs while King profiles are used for dSphs (Ferguson & Binggeli 1994). However, in most cases an exponential law well reproduces even the surface brightness profiles of dSphs (Mateo 1998; Ferguson & Binggeli 1994; Faber & Lin 1983; Hodge et al. 1991a, 1991b; Irwin & Hatzidimitriou 1995). In addition, the luminosity grows with increasing surface brightness in dSphs, similar to that of dIrrs and spirals (Ferguson & Binggeli 1994; Binggeli & Cameron 1991; Bender et al. 1992).

Moreover, both dSphs and dIrrs are dark matter dominated and show an anticorrelation between their mass-to-light ratio and their luminosity (Mateo 1998). Draco and Ursa Minor, the faintest dSphs ($M_B > -10$), have $M/L > 25$ (Lake 1990) and the dimmest dIrrs, GR 8 and Sag DIG ($M_B > -12$) have $M/L \sim 30$.

In summary, the similarities existing between dSphs and dIrrs are enough to postulate an evolutionary link between them. For this to happen, one needs a mechanism that not only removes the cold gas from dIrrs but also drains internal angular momentum and heats the stellar disks.

Supernovae feedback is by far the most widely quoted mechanism to expel gas from dwarf galaxies. In the model by Dekel & Silk (1986), supernovae can induce substantial gas removal in galaxies with a low circular velocity, $V_c \leq 100$ km s^{-1}. For a dwarf dominated by its dark matter halo, any gas loss would have a marginal dynamical effect on the stellar system that is left behind (Navarro, Eke, & Frenk 1996; Burkert & Silk 1997; Gelato & Sommer-Larsen 1999). As a consequence, after star formation has stopped and the galaxy has faded, the "newly born" dSph will maintain the profile and the correlation between luminosity and surface brightness present in its former dIrr state. However, Mac Low & Ferrara (1999), who perform a detailed calculation of the energy balance, have shown that a complete blowout of gas occurs only in very small halos, with $V_c < 15$ km s^{-1}, while, for example, all bright dEs likely reside in substantially more massive halos (Mateo 1998).

An alternative scenario has been proposed, in which the gas is kept hot and star formation is inhibited at high redshift by the photoionizing cosmic UV background in dwarfs with halos corresponding to $V_c \leq 30$ km s^{-1} (Babul & Rees 1992; Efstathiou 1992; Quinn, Katz, & Efstathiou 1996; Bullock, Kravtsov, & Weinberg 2000). The stellar component observed in dSphs would have formed prior to the reionization epoch, while dIrrs would have appeared at low redshift, when the intensity of the background has sufficiently dropped.

However, neither of these mechanisms acts preferentially close to the primary galaxies; thus, no explanation is provided for the morphology-density relation. Moreover, they offer no way to explain the different angular momentum content of the two types of dwarfs.

Among mechanisms related to the local environment, the ram pressure stripping scenario has been invoked frequently for the dwarfs in the Local Group (Einasto et al. 1974; Faber & Lin 1983; van den Bergh 1999; Blitz & Robishaw 2000). A hot gaseous halo surrounding the disk of the Milky Way or M31 would strip the gas from the shallow potential wells of dwarfs moving through (Gunn & Gott 1972). Sophisticated numerical simulations have shown the effectiveness of this mechanism in the inner regions of galaxy clusters such as Coma (Abadi, Moore, & Bower 1999; Quilis, Moore, & Bower 2000). However, observations indicate that the hot gaseous corona of the Milky Way is 3 orders of magnitudes less dense than the core of rich clusters. A recent work by Murali (2000) has shown that a coronal gas density of $n_{\rm H} < 10^{-5}$ cm^{-3}, at 50 kpc, is necessary for the Magellanic Stream not to be dissolved by ram-pressure–driven evaporation in less than 500 Myr. Halo models derived from *ROSAT* X-ray observations yield again comparable upper limits (Kalberla & Kerp 1998) while models in which Local Group dwarfs lose most of their gas because of ram pressure (Gallart et al. 2001; Einasto et al. 1974) require gas densities more than 1 order of magnitude higher. In addition, even if the coronal gas density were substantially larger than currently estimated (e.g., Blitz & Robishaw 2000), ram pressure stripping would be unable to affect the structure and kinematics of the preexisting stellar component.

In galaxy clusters, fast flyby collisions of galaxies with the largest cluster members plus a secondary contribution of the tides raised by the global potential of the cluster are capable of transforming disk galaxies in objects resembling S0 or spheroidal galaxies (Moore et al. 1996b, 1998, 1999a) by removing both mass and angular momentum. This mechanism, known as "galaxy harassment" affects all galaxy components and is purely gravitational. For harassment to be effective, 3–4 collisions per galaxy with a galaxy as massive as the Milky Way (having a circular velocity $V_c \sim 220$ km s^{-1} corresponding to ~ 0.15 of the circular velocity $V_{\rm clus} \sim 1500$ km s^{-1} of a Coma-sized cluster) are required. This occurs in clusters, in which the collision rate $\mathcal{R}$ is around 1 Gyr^{-1}, as follows from $\mathcal{R} = N\sigma S$, where N is the number density of Milky Way–sized galaxies (~ 30 Mpc^{-3}) in a rich Coma-like cluster (of radius ~ 1.5 Mpc), σ is the velocity dispersion of the cluster (~ 1000 km s^{-1}), and S is the cross section of the target galaxy (here we are considering the extent of a typical L_* galaxy out to the virial radius of the dark matter halo, ~ 300 kpc, as it will take a few Gyr for a galaxy to approach the cluster core and be tidally truncated significantly). Rescaling the calculation to the case of a Local Group dwarf satellite of either the Milky Way or M31 colliding against a fairly large satellite with $V_c \geq 30$ km s^{-1} (namely, comparable to the Small Magellanic Cloud and having $V_c \sim 0.15 V_{\rm MW}$, where $V_{\rm MW}$ is the circu-

lar velocity of the Milky Way), one obtains only $\mathscr{R} < 0.1$ Gyr^{-1}. This is because the number of observed satellites in the halo of the Milky Way or M31 is much lower than the number of Milky Way–like galaxies in clusters (Moore et al. 1999b; Klypin et al. 1999). Thus, unless we are missing a substantial population of satellites, either because they are completely dark or because their baryons have not yet been turned into stars due to some mechanism that inhibits cooling (Blitz et al. 1999), harassment is negligible in the Local Group.

If close-by encounters between dwarfs are rare in the Local Group, only the tidal field of the primary halos can substantially reshape these small galaxies. Kuhn & Miller (1989) and Kuhn (1993) argued, on the basis of a series of numerical experiments, that Galactic tides could severely heat the dwarf satellites if a resonant coupling between their orbital motion and their internal pulsation frequency occurs. They claimed that dSphs could be unbound systems with no dark matter, their apparent large velocity dispersions arising because of the disruption of the systems at the present time. Similar results were reached Kroupa (1997) and Klessen & Kroupa (1998). More recently, Gnedin et al. (1999) found, using a generalized semianalytical formulation based on the impulsive approximation and inclusive of adiabatic corrections, that the heating of a satellite by the tides of the primaries can be very strong when the orbits are eccentric or have pericenters close to the core of the primary. These results are also supported by the more sophisticated time-dependent perturbation theory of gravitational shocks developed by Weinberg (1994a, 1994b, 1994c). Typical orbits of subhalos in structure formation models are fairly eccentric, having an average apocenter to pericenter ~ 5 (Ghigna et al. 1998). The orbital time in the Milky Way halo is roughly the same as in a Coma-like cluster, as $T_{\rm orb} \sim 2\pi R/V_c$ and $R \propto V_c$ for virialized structures (White & Frenk 1991) and is ~ 3 Gyr for an object on a circular orbit halfway from the center of the larger system. However, the Milky Way satellites were allowed a higher number of orbits than galaxies in virialized clusters because the latter typically appeared 5 Gyr ago (Rosati et al. 2001), whereas the Galaxy was already in place at least 10 Gyr ago (van den Bergh 1996).

Semianalytical approaches limit the analysis to the amount of energy that can be injected by tides into a satellite, being not able to handle the nonlinear mechanisms possibly excited by such energy input, namely, gravitational instabilities in the stellar component, that can lead to substantial morphological evolution. In Mayer et al. (2001), we investigated for the first time the fate of "tidally stirred" dwarf irregulars orbiting the halo of the Milky Way using high-resolution N-body/smoothed particle hydrodynamic (SPH) simulations. We found that the general properties of their remnants well match those of the dSphs and dEs in the Local Group, providing, in addition, a natural explanation for their observed morphological segregation. In this paper, we carefully describe the techniques used to construct realistic replicas of dwarf irregulars and we study in depth their dynamical evolution and the internal structure of their remnants. In addition, by carrying out an unprecedented number of high-resolution N-body simulations (more than 50), we explore a much wider parameter space in terms of both orbital parameters and internal structure of the satellites, obtaining a statistical sample for a detailed comparison with observations. Finally, our present study aims at identifying the basic conditions for tidal stirring to be effective as well as at testing against observations the predictions to which it gives rise within the framework of hierarchical structure formation. The simulations were performed with PKDGRAV (J. Stadel & T. Quinn 2001, in preparation; Dikaiakos & Stadel 1996), a fast, parallel binary treecode, or, when a gas component is also included, with a newer version of the same code, GASOLINE, which implements an SPH algorithm for solving the hydrodynamical equations and radiative cooling (J. Wadsley, J. Stadel & T. Quinn 2001, in preparation).

The outline of the paper is as follows. In §§ 2 and 3, we illustrate, respectively, the initial dwarf galaxy models and orbital configurations. In § 4, we follow the dynamical evolution of the satellites, while § 5 is devoted to the structural properties of the remnants. In § 6 we test the tidal stirring scenario, varying the internal structure of the satellites, the orbits, and the structure of the primary halo. In § 7 we derive the star formation history of the satellites; § 8 discusses the final distribution of cold gas, whereas § 9 concerns the gross observational properties of the remnants. Finally, in § 10 we discuss the main results and draw our conclusions.

2. MODELS OF SATELLITES

The models of dwarf irregular galaxies are constructed using the technique by Hernquist (1993), which has been extensively shown to produce stable configurations for systems with more than one component. In this work, galaxies normally comprise an exponential stellar disk embedded in an extended truncated isothermal dark matter halo. In addition, in some cases, a cold gas component is also present in the disk. The profile of the dark matter halo is given by

$$\rho_h(r) = \frac{M_h}{2\pi^{3/2}} \frac{\alpha}{r_c} \frac{\exp\left(-r^2/r_t^2\right)}{r^2 + r_c^2}, \tag{1}$$

where M_h is the halo mass, r_t serves as a cutoff radius, r_c is the "core" radius, and α is a normalization constant defined by $\alpha = \{1 - \sqrt{\pi q}\exp(q^2)[1 - \mathrm{erf}(q)]\}^{-1}$, where $q = r_c/r_t$. The stellar disks initially follow the density profile (in cylindrical coordinates)

$$\rho_d(R, z) = \frac{M_d}{4\pi r_h^2 z_0} \exp\left(-R/r_h\right) \mathrm{sech}^2\left(\frac{z}{z_0}\right), \tag{2}$$

where M_d is the disk mass, r_h is the radial scale length, and z_0 is the vertical scale thickness.

The particles used to represent the gaseous disk follow roughly the same density profile of the disk stars but their vertical scale height depends on the temperature of the gas. For a gas temperature $T = 10^4$ K, the gas layer is thinner than the stars for vertical stellar dispersions similar to those in the Milky Way disk.

Our procedure for "building" dwarf galaxies involves the joint use of observations and theoretical models of structure formation. We build two basic galaxy models, one of a high surface brightness (HSB) dwarf and one of a low surface brightness (LSB) dwarf (LM1 and HM1, respectively), and then we obtain slightly different versions of those by keeping fixed the mass of their various components and varying the other structural parameters (§ 2.1). In addition, we construct models with different masses (§§ 2.2 and 2.3)

using the scaling relations for objects forming in cold dark matter cosmogonies (e.g., Mo, Mao, & White 1998).

2.1. *Models at Fixed Mass*

In a scenario in which galaxies form from the cooling of gas inside dark matter halos (White & Rees 1978; White & Frenk 1991), the baryons settle into a disk rotating in centrifugal equilibrium within the halo and, thus, the rotational velocity equals the circular velocity of the halo. Therefore, once we fix the circular velocity V_c of the halo, we determine the luminosity of the embedded disk according to the Tully-Fisher relation. For our basic models, we choose a halo circular velocity $V_c = 75$ km s^{-1}. Zwaan et al. (1995) have shown that high surface brightness (HSB) and low surface brightness (LSB) disk galaxies obey the same Tully-Fisher (T-F) relation in the B band (although LSBs show more scatter), $L_B \sim V_c^4$. A rotational velocity of 75 km s^{-1} implies $M_B \sim -18$ according to the T-F relation: these parameters correspond to the brightest dwarf irregular galaxy in the Local Group, the LMC (Mateo 1998; Sofue 1999).

To satisfy the same T-F relation, LSBs must have larger disk scale lengths compared with those of equally luminous HSBs because $L \propto \Sigma_d r_h^2$ (where Σ_d is the surface luminosity). For the disk scale length r_h of the HSB, we chose a value of 2 kpc, while the LSB model has a disk scale length of 4.8 kpc: both values are in agreement with the bimodal V_c-r_h relation in Zwaan et al. (1995). To fix the disk mass, we follow Bottema (1997); thus, we assume $(M/L)_{*B} = 2$, which yields $3.22 \times 10^9\ M_\odot$ for the mass of the stellar disk of both HSB and LSB models.

Once the circular velocity is known, the virial mass M_{200} and virial radius R_{200} of the halo (which we equate to the tidal radius r_t in all our models) follow immediately from

$$M_{200} = \frac{V_{200}^3}{10GH(z)} \quad \text{and} \quad R_{200} = \frac{V_{200}}{10H(z)} \tag{3}$$

where, for the basic models, we assume $z = 0$ and $H(z) = H_0 = 50$ km s^{-1} Mpc^{-1} The normalization in the above equations follows from assuming that the critical overdensity for the collapse of objects is $200\rho_c$, where ρ_c is the critical density of the universe, as appropriate for a standard cold dark matter (SCDM) cosmology. In other more currently favored models, such as a cold dark matter model with a dominant cosmological constant, the value of the critical overdensity is marginally different; thus, the final sizes and masses of halos are barely affected (Eke, Cole, & Frenk 1996). According to equation (1), we assign to our basic dwarf galaxy models a (halo) virial mass $M_{200} = 1.6 \times 10^{11}\ M_\odot$ and a virial radius $R_{200} = r_t = 150$ kpc.

By changing the *concentration* $c = r_t/r_c$ at fixed r_t and halo mass, we reproduce the rotation curves of both LSB and HSB dwarfs, as done by de Blok & McGaugh (1997) for a large sample of galaxies of both types (see also Persic & Salucci 1997). Following again the same authors, we assume that the halo and disk scale lengths are related and set $r_c = r_h$, thus making HSB halos more than twice as concentrated as LSB halos given the difference in their disk scale lengths. We also build two models in which r_h and r_c are not equal to further explore the parameter space. The rotation curves of the basic HSB and LSB models (LM1 and HM1) and of the latter two models (LM1rc03 and HM1rc03) are shown in Figure 1.

In the models described so far, the scale height of the disk is fixed at $0.1r_h$, as suggested by observations of late-type galaxies (Van der Kruit & de Grijs 1999; de Grijs, Peletier, & Van der Kruit 1997), and we set $Q = 2$ at $r = 2.5r_h$. We recall that Q is the Toomre stability parameter for rotationally supported stellar disks, $Q = \sigma_r \kappa/3.36G\Sigma$, where σ_r is the radial velocity dispersion, κ is the epicyclic frequency, and Σ is the surface density of the disk, and each of these quantities is a function of radius R. Our models have $Q \geq 2$ throughout most of the disk, a condition necessary for avoiding the spontaneous growth of bars (Athanassoula & Sellwood 1986; Friedli 1999).

Different choices of Q and z_s can determine, respectively, a different susceptibility to the growth of bars and to bending instabilities, the latter being vertical oscillations responsible, for instance, for the buckling of bars (Merritt & Sellwood 1994; Raha et al. 1991). Given the chosen parameters, the basic models have structurally normal disks: to further explore the issue of instabilities, we construct a small set of models with different values of Q and z_s. The rotation curves are not affected by the latter variation of parameters, and they look the same as those of models LM1 and HM1 shown in Figure 1.

Figure 2 shows the stability properties of the various models employed (including the model of GR 8 described in § 2.3) in terms of Q and $X_2 = \kappa^2 R/4\pi G\Sigma$. In Table 1, the corresponding structural parameters are listed. N-body simulations by Mihos, McGaugh, & de Blok (1997) have shown that in encounters of equal-mass galaxies, $X_2 > 1$ in the inner disk is a sufficient condition for systems with slowly rising rotation curves, such as those of LSBs, to be stable against bar formation, while $X_2 > 3$ is required for disks with steep rotation curves, such as those of HSBs. Since in our simulations, the perturber's mass (the Milky Way) is at least 30 times larger than the mass of the target dwarf galaxy, we will be able to test the validity of this criterion in a radically different situation. Finally, we will test the susceptibility to vertical bending instabilities with model LMH (Table 1), which is identical to model LM1 except for a larger scale height ($z_s = 0.3r_h$): this should suffer little vertical heating (see Raha et al. 1991).

2.2. *Rescaled Models*

To fix the parameters of model galaxies with different (smaller) masses, we choose a value for the new mass and then we make use of equation (3) to determine the new circular velocity V_{200} and virial radius R_{200} of the dark matter halo *assuming* $z = 0$ *and thus* $H(z) = H_0$. The disk masses and scale lengths are assumed to simply follow the halo scaling (Mo et al. 1998).

As shown by equation (3), masses and radii of objects formed in hierarchical cosmogonies depend on redshift *at fixed circular velocity*. The scaling is contained in the Hubble constant (we assume $\Omega_0 = 1$ and $\Lambda_0 = 0$ as in SCDM, but the scaling would be marginally different for a flat universe with a nonzero cosmological constant as in the currently popular LCDM model),

$$H(z) = H_0[\Lambda_0 + (1 - \Omega_0 - \Lambda_0)(1 + z)^2 + \Omega_0(1 + z)^3]^{1/2}\ , \tag{4}$$

and implies that radii and masses decrease at the same rate, i.e., $\sim (1 + z)^{-3/2}$. As a consequence, the density of objects grows as $(1 + z)^3$. Some of the dwarf spheroidal galaxies inhabiting the Local Group today must have formed at $z = 1$ or higher given the very old age of the bulk of their stellar populations. Therefore, we also build models with

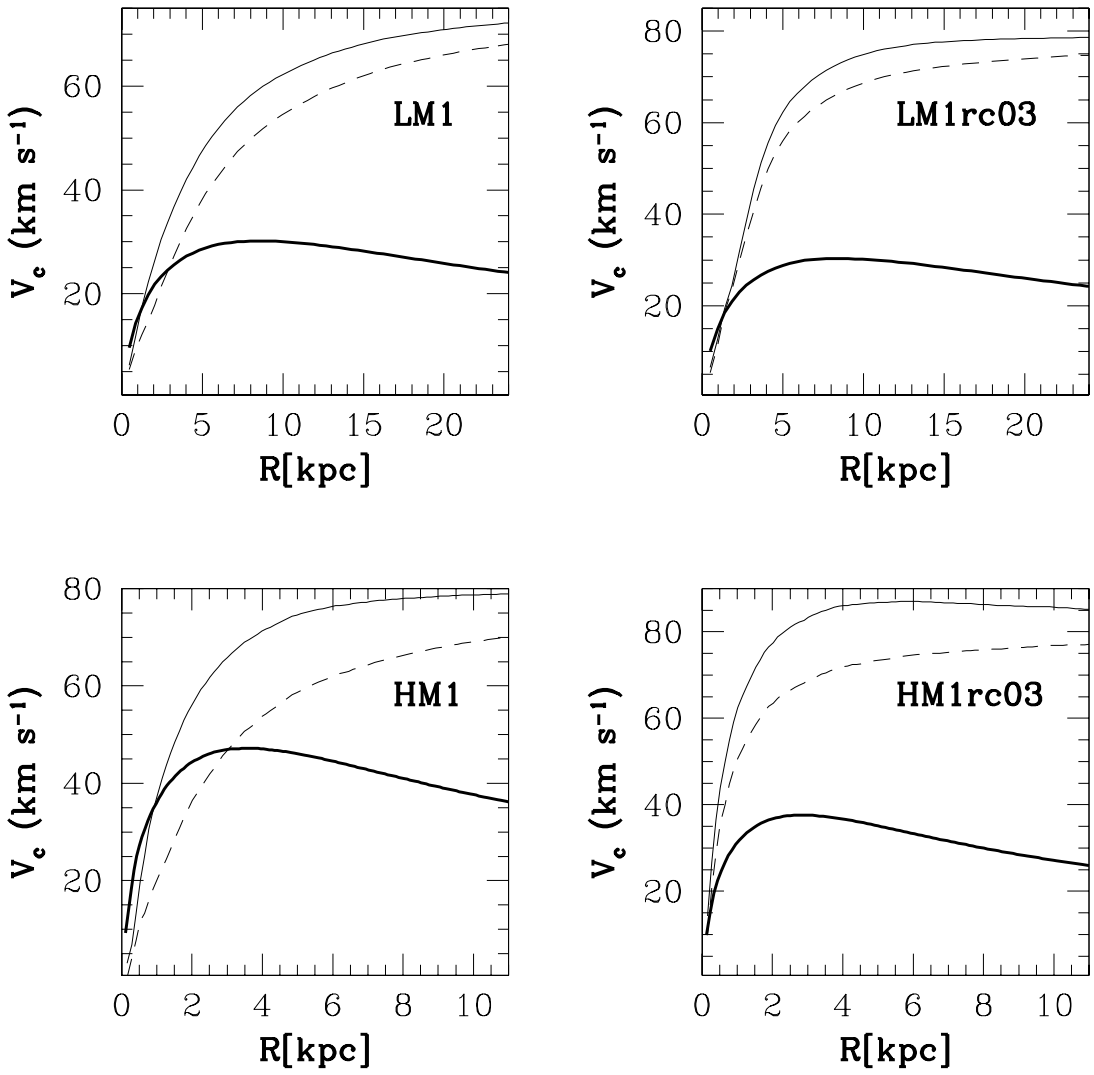

FIG. 1.—Rotation curves of the basic LSB and HSB models plotted out to $5r_h$. Rescaled models (see text) have rotation curves like those of models LM1 and HM1, albeit with different intrinsic scales. The thin dashed line and thick solid line represent the separate contribution of, respectively, dark matter and stars, while the thin solid line represents their sum (see Table 1 for details).

masses and radii rescaled as they were formed at $z = 1$ (models LZ and HZ) to investigate how the scaling with redshift implied by the hierarchical scenario can affect their evolution (see Table 1).

The intrinsic stability properties of all these rescaled models are unvaried with respect to the basic models because equations (3) and (4) define an invariant transformation for both Q and X_2. The structural parameters of all the rescaled models can be viewed in Table 1: Their rotation curves look exactly the same as those of the basic models shown in Figure 1, albeit on a different scale.

2.3. *The GR8 Model*

So far, we have used the Tully-Fisher relation to link circular velocities of halos to luminosity. Hoffman et al. (1996) have shown that the T-F relation exhibits a large scatter at $M_B \geq -12$. The cosmological scaling offers an attractive alternative to set the physical parameters for models of the faintest dwarf irregular galaxies. Examples of very faint dIrrs are found in the Local Group; both GR 8 and Sag DIG have $M_B > -12$. It turns out that galaxies that faint should correspond to halos with $M_{200} < 10^9\ M_\odot$ and that such halos form typically at $z \geq 2$ (Lacey & Cole 1993, 1994).

We build a model resembling the GR 8 dwarf. We use the kinematics of the gas at large radii to construct the global potential of the dwarf. At 2–3 disk scale lengths, the neutral hydrogen in GR 8 is pressure supported, with a peak velocity dispersion $\sigma \sim 12$–13 km s^{-1} (Carignan et al. 1990). Assuming that the gas is in virial equilibrium with a surrounding isothermal dark matter halo, the latter should have a virial circular velocity $V_{200} = \sqrt{2}\sigma \sim 17$ km s^{-1}. This fixes the virial mass and virial radius of the halo through equations (3) and (4), which are evaluated for $z = 2$. The disk scale length (76 pc) and stellar disk mass (1.6×10^6 $M_\odot$) are the observed values (Carignan et al. 1990). The chosen r_h and R_{200}, assuming as always $r_c = r_h$, imply a very concentrated halo and a very high halo/disk mass ratio (see Table 1).

The resulting central dark matter density is very high, $\sim 0.3\ M_\odot$ pc^{-2}. This value is slightly higher than inferred for GR 8 ($0.07\ M_\odot$ pc^{-2}) but similar to that inferred for Draco and Ursa Minor (Lake 1990; Mateo 1998). The mass-to-light ratio at the optical radius ($\sim 3r_h$) is ~ 32, like

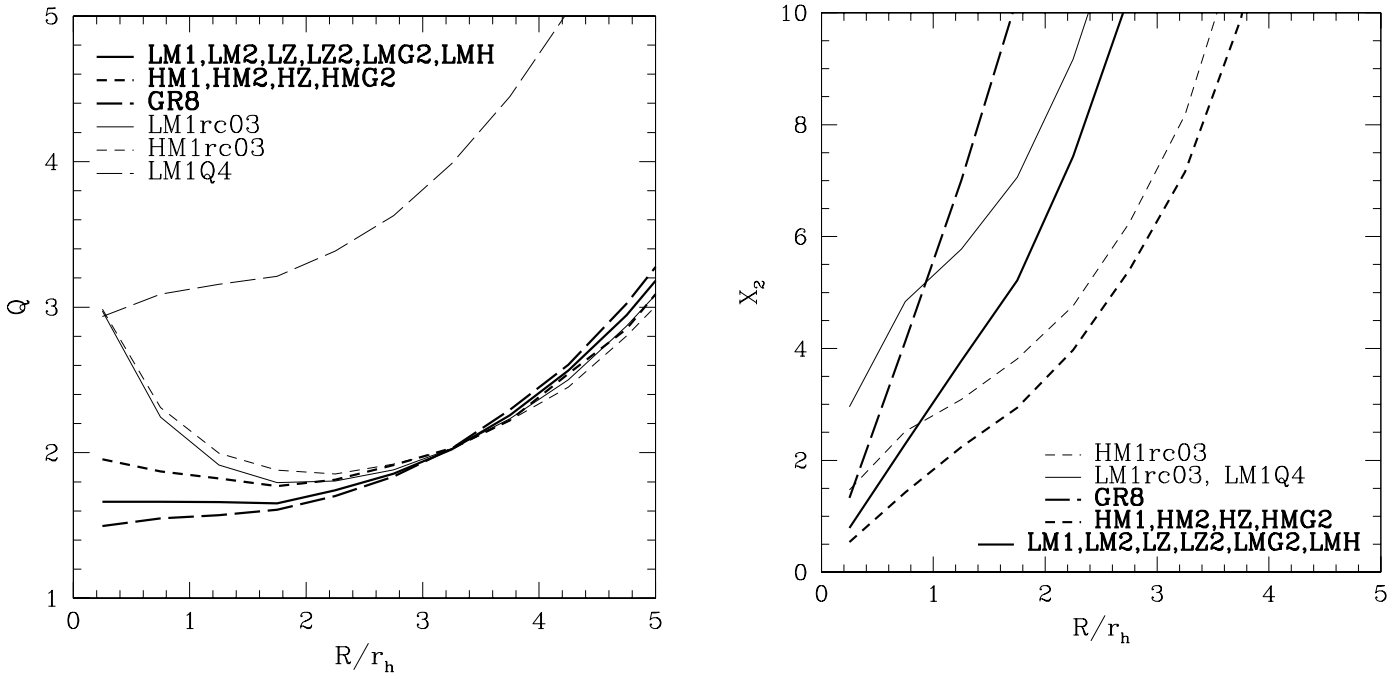

FIG. 2.—Q and X_2 parameters as a function of distance (in units of the disk scale length) for various models (see Table 1 for details on the models)

that of GR 8, not counting the contribution of the gaseous disk. The rotation curve of the "GR 8" model is shown in Figure 3.

2.4. *Models with a Gas Component*

We also construct an LSB and an HSB model with a cold gaseous disk that should represent the neutral hydrogen present in observed dwarf irregular galaxies. Dwarf irregular galaxies are generally gas-rich, with an average total H I–to–stellar mass ratio larger than one (Hoffman et al. 1996). However, the gaseous disks are typically two times more extended than the stellar disks (Cote, Freeman, & Carignan 1997; de Blok & McGaugh 1997; Young & Lo 1997), whereas within the optical radius (~3 disk scale lengths), the neutral hydrogen fraction often drops to less than 50% of the stellar mass (Jobin & Carignan 1990; Cote et al. 1997). As we will show, material lying outside $3r_h$ is almost entirely stripped when the satellites orbit in the Milky Way halo and thus would not affect the bound components. Therefore, the gaseous disk included in our model galaxies extends only out to the radius of the stellar disk, and its mass is 30% of the total baryonic mass. The total disk mass (stars + gas), as well as all the other structural parameters, are shown in Table 1 (models LMg2 and HMg2). The density drops to zero at a radius $R < 0.5r_h$ to mimic the "holes" in neutral gas distribution existing in the

TABLE 1

MODELS OF SATELLITES

Model	M_{200}/M_P	M_d/M_{200}	$(M_{200}/M_d)_{\rm opt}$ $(M_\odot/L_\odot)$	r_c/r_t	r_t (kpc)	r_h (kpc)	V_c (km s^{-1})	μ_{0B}	$Q_{\rm opt}$	X_2
HM1 (HSB)	0.032	0.016	6	0.02	140	2	75	22	2	2
HM2 (HSB)	0.01	0.016	6	0.02	95	1.35	50	22.5	2	2
HMg2 (HSB)	0.01	0.016	6	0.02	95	1.35	50	22.5	2	2
HZ (HSB)	0.013	0.016	6	0.02	49.5	0.7	75	21.5	2	2
HM1rc03 (HSB)	0.032	0.016	10	0.006	140	2	75	22	2	2.7
LM1 (LSB)	0.032	0.016	12	0.036	140	4.8	75	24	2	3
LMH (LSB, $z_s = 0.3r_h$)	0.032	0.016	12	0.036	140	4.8	75	24	2	3
LM2 (LSB)	0.01	0.016	12	0.036	95	3.2	50	24.5	2	3
LMg2 (LSB)	0.01	0.016	12	0.036	95	3.2	50	24.5	2	3
LZ (LSB)	0.013	0.016	12	0.036	49.5	1.69	75	23.5	2	3
LZ2 (LSB)	0.013	0.016	12	0.036	16.5	0.563	25	24.6	2	3
LM1rc03 (LSB)	0.032	0.016	15	0.0108	140	4.8	75	24	2	5
LM1Q4 (LSB)	0.032	0.016	12	0.036	140	4.8	75	24	4	3
GR8	1.38×10^{-4}	2.174×10^{-3}	32	0.014	7.8	0.076	17	22.5	2	6

NOTE.—The structural parameters of the dwarf galaxy models are shown. M_p is the mass of the Milky Way halo, M_d is the mass of the satellite's disk, while M_{200} is the virial mass of the halo of the satellite; r_t is the truncation radius of its halo ($= R_{200}$), r_h is its disk scale length, and r_c is its halo core radius. The circular velocity V_c is measured at the virial radius of the satellite (i.e., $V_c = V_{200}$). The mass-to-light ratio at the optical radius ($= 3r_h$) is $(M_{200}/M_d)_{\rm opt}$ and μ_{0B} is the B-band central surface brightness in mag arcsec^{-2}. Model LMg2 and HMg2 have a gaseous component in the disk, with mass $M_g = 0.35\ M_d$. The stability parameter X_2 is estimated at r_h, while Q is estimated at the optical radius.

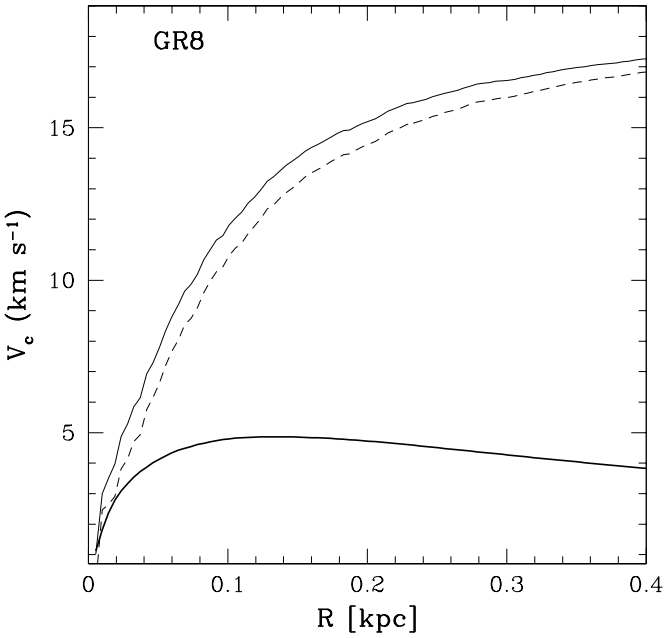

FIG. 3.—Rotation curve of the GR 8 model plotted out to $5r_h$. The thin dashed line and thick solid line represent the separate contributions of, respectively, dark matter and stars, while the thin solid line represents their sum (see Table 1 for details).

center of dwarf irregular galaxies (Cote et al. 1997). The temperature of the gas is fixed at 5000 K after stability tests in the adiabatic regime. The rotation curves of both models are shown in Figure 4.

2.5. *Numerical Stability of the Models*

N-body simulations are subject to two-body relaxation effects. These can be particularly severe when more systems of different masses or a system of several components are present. Massive halo particles may heat up the disk even in absence of any external perturbation by colliding with lighter stellar or gas particles: a similar numerical effect is known to be responsible for the premature evaporation and disruption of small subhalos in cosmological simulations with insufficient resolution (Moore, Katz, & Lake 1996a; Moore et al. 1999a; Knebe et al. 2000). To minimize numerical disk heating, we use lighter halo particles in the central part of the halo (precisely within 10 disk scale lengths) where orbital times are shorter and therefore collisions with disk particles are more frequent. We perform several tests in isolation to find the optimal balance between a reasonable stability and a moderate total number of particles (see Fig. 5).

The final models have a disk of 50,000 particles while the halo is sampled by 208,350 in the LSB model and 180,860 in the HSB model (the high-resolution halo component in the LSB extends to a larger fraction of the virial radius because the stellar disk does likewise, resulting in a higher total number of particles). For the GR 8 model, we had to use more than 3×10^6 particles in the halo because of the exceptionally high halo/disk ratio: This is the *highest resolution model ever made for a single galaxy*, with a single particle weighting only $\sim 50\ M_\odot$. The softenings in the models are a fixed fraction of the disk scale length, thus ensuring the same *intrinsic* spatial resolution for HSBs and LSBs as well as for all their rescaled versions. In code units (for which $r_h = 1$), they are $s_d = 0.06$ for the disk, $s_{h1} = 0.32$ for the high-resolution halo and $s_{h2} = 0.4$ for the low-resolution halo. Time steps in our simulations (which adopt a multistepping criterion) can be as small as $0.01t_{\rm cd}$, where $t_{\rm cd}$ is the crossing time of the disks at $r = r_h$. In the gas-dynamic runs, radiative cooling is implemented for a primordial mixture of hydrogen and helium. We adopt a cooling function similar to that in Hernquist & Katz (1989), based on which cooling drops significantly below 10^4 K. We use 20.000 particles to sample the gas component and 40.000 particles for the stellar disk, minimizing any eventual collisional heating of the gaseous disk by the star particles as $M_{\rm gas}/M_{\rm stars} \sim 0.3$ (otherwise two-body heating by stellar or dark particles may suppress radiative cooling of the gas; see Steinmetz & White 1997). Halos, in this case, have 250.000 particles in total.

3. INITIAL CONDITIONS

The satellites are placed on bound orbits in the potential of a Milky Way–sized primary halo. The latter is modeled as the fixed potential of an isothermal sphere with a total mass $4 \times 10^{12}\ M_\odot$ inside a virial radius $R_{\rm vp} = 400$ kpc, consistent with both recent measures based on radial velocities of distant satellites (Wilkinson & Evans 1999) and with generic models of structure formation (Peebles et al. 1989). The core radius is 4 kpc and the resulting circular velocity at the solar radius is 220 km s^{-1}. Dynamical friction is neglected because orbital decay times are expected to be longer than the Hubble time given the small mass of the satellites (they are at least ~ 30 times less massive than the primary) and the delay introduced by tidal stripping (Colpi, Mayer, & Governato 1999).

In the majority of the runs, which we will call the "standard runs," the orbits have an apocenter close to the virial radius of the Milky Way halo, in agreement with the results of *N*-body simulations of structure formation (Ghigna et al. 1998). The same simulations also show that the orbits of satellites have an average apo/peri ~ 5, while sporadic measurements of the orbits of Local Group dSphs yield, although with large errors, nearly circular orbits, with average apo/peri = 2 (Schweitzer et al. 1995; Ibata & Lewis 1998). To maintain consistency with theoretical expectations as well as with observations, we explore mainly orbits with apo/peri between 4 and 10, but we also consider orbits with apo/peri as low as 1.5–2. The orbital energy $E_{\rm orb}$ is usually such that the corresponding circular orbit would have a radius $\sim 0.5R_{\rm vp}$ and a typical period of ~ 3 Gyr. We will refer to these orbits as the *standard orbits*. As the orbits considered typically have pericenters larger than 40 kpc, the contribution of the Milky Way disk to the primary potential should be negligible: we will show the validity of this hypothesis by adding an external axisymmetric potential in a few runs.

Satellites that entered the Milky Way halo at high redshift ($z \geq 1$) became bound on orbits with a significantly smaller apocenter compared with satellites infalling later because the primary halo itself was typically 2–3 times smaller (see eqs. [3] and [4]). Therefore, we also consider the regime of *tightly bound orbits*, with apocenters ranging from $\frac{1}{2}$ to $\frac{1}{3}$ of the present-day virial radius of the Milky Way halo, thus having a orbital energy $E_{\rm orb}$ lower than that of the standard orbits.

The inclination of the disk spin with respect to the orbital angular momentum is also varied, going from direct to

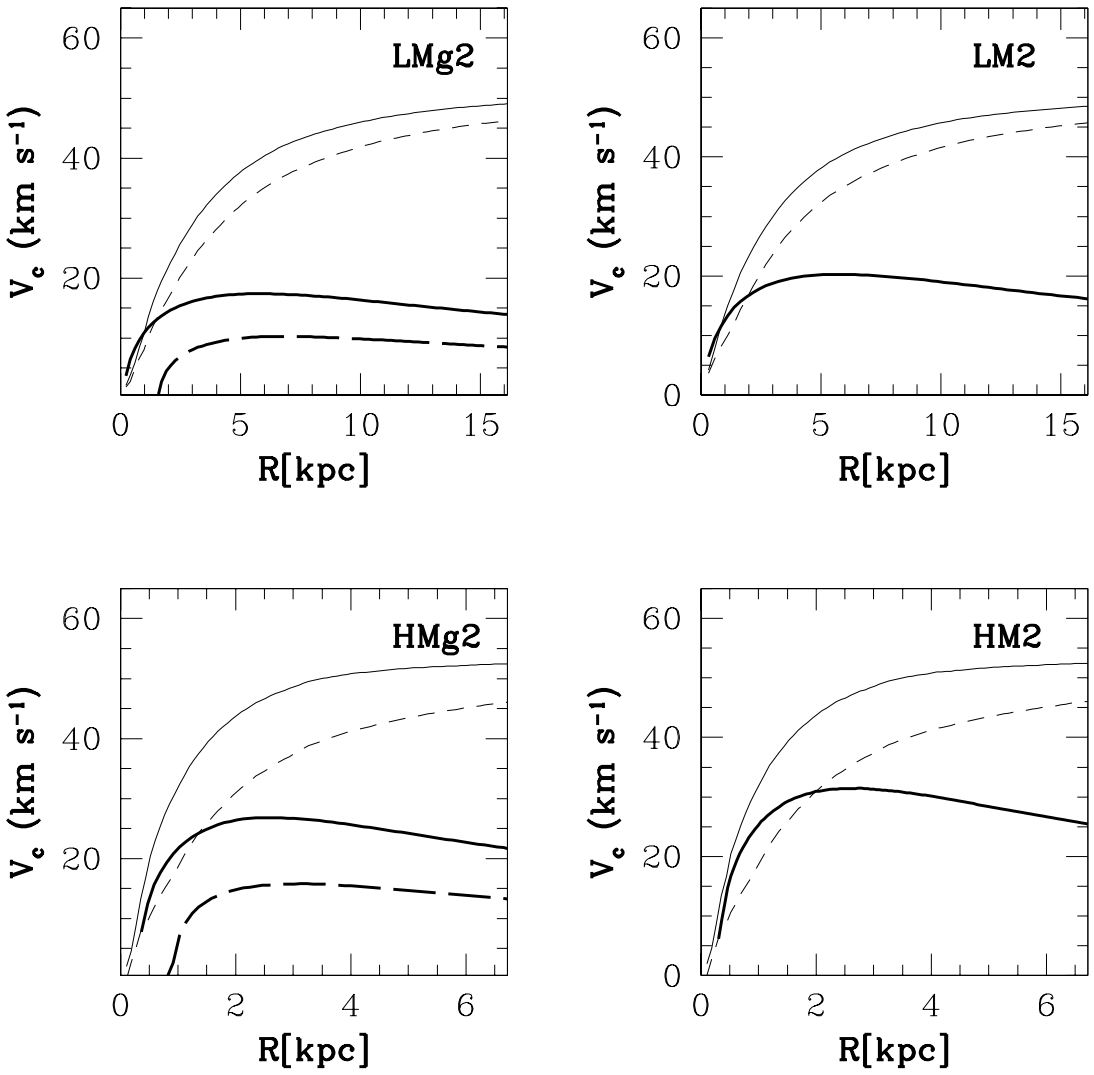

FIG. 4.—Rotation curves of models including a gaseous component along with those of their gas-free counterparts plotted out to $5r_h$. The thin dashed line and thick solid line represent the separate contributions of, respectively, dark matter and stars; the thick dashed line represents the separate contribution of gas while the thin solid line represents the total rotation curve, including all the components (see Table 1 for details).

retrograde spin-orbit orientations. The combination of different orbital parameters and different models of satellites has led us to perform more than 50 high-resolution runs. Figure 6 shows the parameter space covered by our simulations in terms of both initial models and orbital configurations. The orbital parameters and satellite models employed in the various runs are indicated in Tables 2 and 3.

4. DYNAMICAL EVOLUTION

4.1. *Collisionless Runs*

Dwarf galaxy models are evolved for several gigayears in the external potential of the Milky Way halo. The strong tidal disturbance exerted by the primary halo produces a dramatic morphological evolution of the small satellites after 2–3 pericenter passages, corresponding to 7 Gyr on the standard orbits. The satellites are first tidally truncated down to the radius imposed by their pericenter distance and then continue to lose mass as each subsequent tidal shock pumps energy into them and loosens their potential wells (Gnedin & Ostriker 1999).

In general, LSBs lose more than 90% of their halo mass and $\sim 60\%$ of their stellar mass, while HSBs, although still losing most of their halo mass, retain, on average, at least 70% of their initial disk mass. A high-density dwarf model such as GR 8 is barely perturbed on a standard orbit (run GR81), while it loses $\lesssim 5\%$ of its disk mass but most of its outer halo mass if it falls on a short-period, tightly bound orbit ($T_{\rm orb} \sim 1.3$ Gyr) as expected at $z \geq 1$ (see previous section), performing five pericenter passages in less than 7 Gyr.

The evolution of the mass distribution for the various models is reflected in the variation of the circular velocity profiles (Figs. 7, 8, 9). After 7 Gyr, LSBs have stellar masses of $\sim 10^8\ M_\odot$ while HSBs have stellar masses closer to $10^9\ M_\odot$. LSBs are more fragile than HSBs both because they have a low-concentration halo and because they have large disk scale lengths. For the same disk mass, the difference in scale length is a factor of 2.4. Correspondingly, if t_c is the crossing time at the disk half-mass radius and $t_{\rm enc} = R_{\rm peri}/V_{\rm peri}$ is the encounter time (namely, the time spent close to pericenter $R_{\rm peri}$ while moving at the velocity $V_{\rm peri}$) for $R_{\rm peri} \sim 40$ kpc as in most of the cases (see Tables 2 and

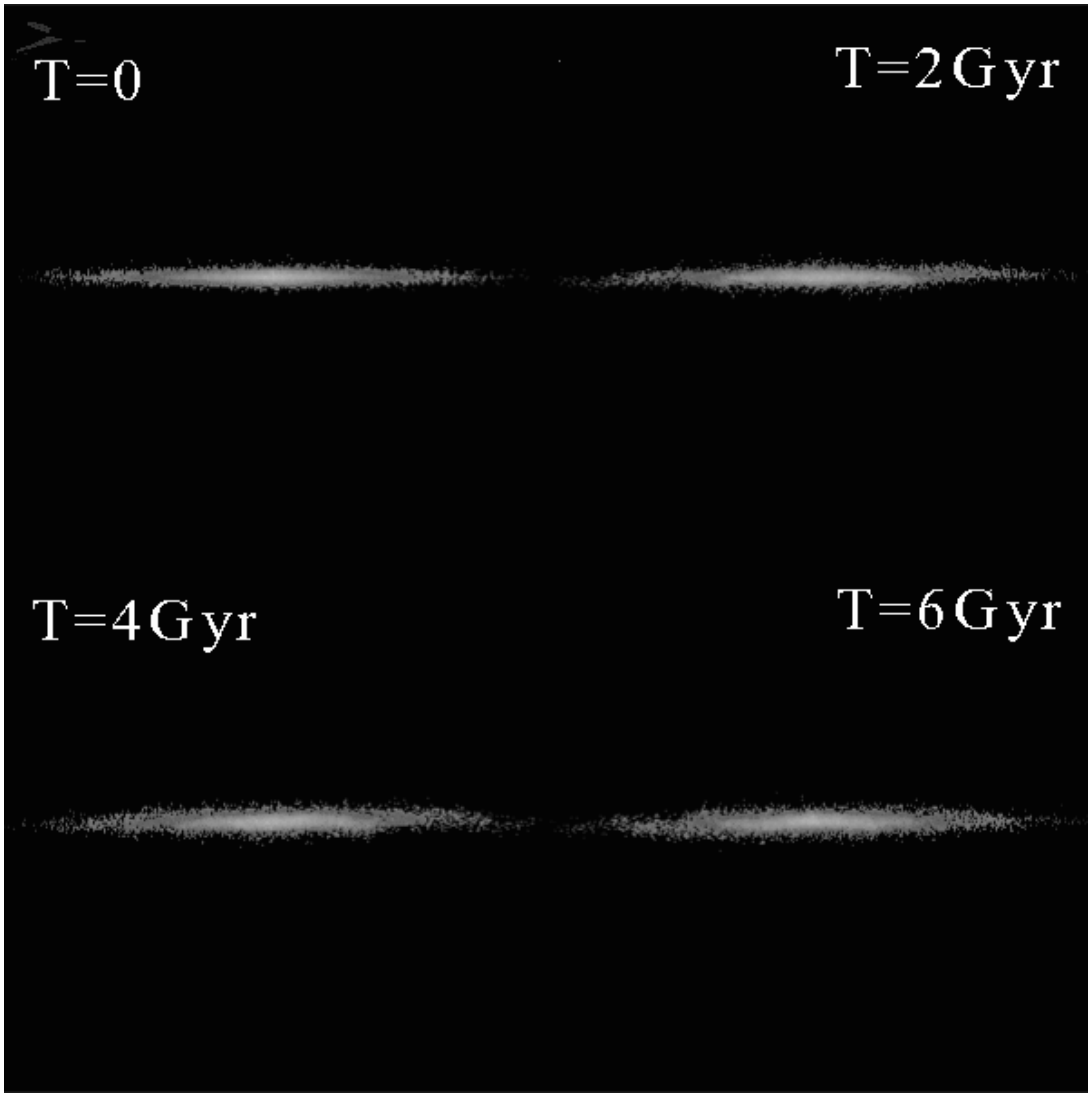

FIG. 5.—Evolution in isolation of the disk model LM1. Shown is the edge-on color-coded logarithmic density (the darker the color, the lower the density). At $T = 3.5$ Gyr, a weak warp is apparent. The boxes are 30 kpc on a side.

3), we have $t_c/t_{\rm enc} \sim 1$ for the LSBs, while $t_c/t_{\rm enc} < 1$ for the HSBs; thus, the latter will respond more adiabatically to the perturbation (Gnedin et al. 1999). Orbits with progressively larger pericenters obviously produce a lower damage even in LSBs. Finally, limited stripping occurs in HZ and LZ models that have a disk scale length 2.83 times smaller than their $z = 0$ counterparts (Figs. 7 and 8).

Close to the first pericentric passage, both LSBs and HSBs develop a central bar, its scale length being always $\sim r_h$. The higher intrinsic stability of LSBs to bar formation (suggested by the X_2 parameter in Fig. 2) is clearly not indicative when the perturber, namely, the Milky Way, is several times more massive than the target satellite, as was also argued by Miwa & Noguchi (1998). The GR 8–like model develops very extended spiral arms after the first tidal shock. The second shock triggers the formation of a central bar that is more compact than usual, being $\sim 0.5 r_h$ in length.

The appearance of the bar structure corresponds to a drastic change of the orbits of stars inside the bar radius: nearly circular orbits turn into nearly radial box or tube orbits supporting the elongation of the bar. This change is illustrated in Figure 10, where the specific angular momentum of stars inside r_h is plotted against time. The bar leads to an increase in the central concentration of the stellar density profiles, as is explained in the next section. However, the degree of central concentration may vary depending on the strength of the bar. In the case of LSBs, the bar is weakened by tidal stripping as stars are removed even inside the bar radius when the pericenter distance is below 50 kpc (e.g., run L01). Instead, for larger pericenters or for satellite models with smaller initial disk scale length and/or higher central densities (all HSB models and also LZ models), the bar is quite stable to stripping.

The rotating bar soon slows down, shedding angular momentum outward to the halo and outer stellar material as a result of dynamical friction (Hernquist & Weinberg 1989; Fux, Martinet, & Pfenninger 1995). In the meantime, stripping removes the high-angular momentum stellar material outside the bar radius.

The bar starts to buckle soon after the first orbit, when the radial anisotropy has increased in such a way that $\sigma_z/\sigma_p \leq 0.4$, where σ_z and σ_p are, respectively, the velocity dispersion normal and parallel to the plane defined by the

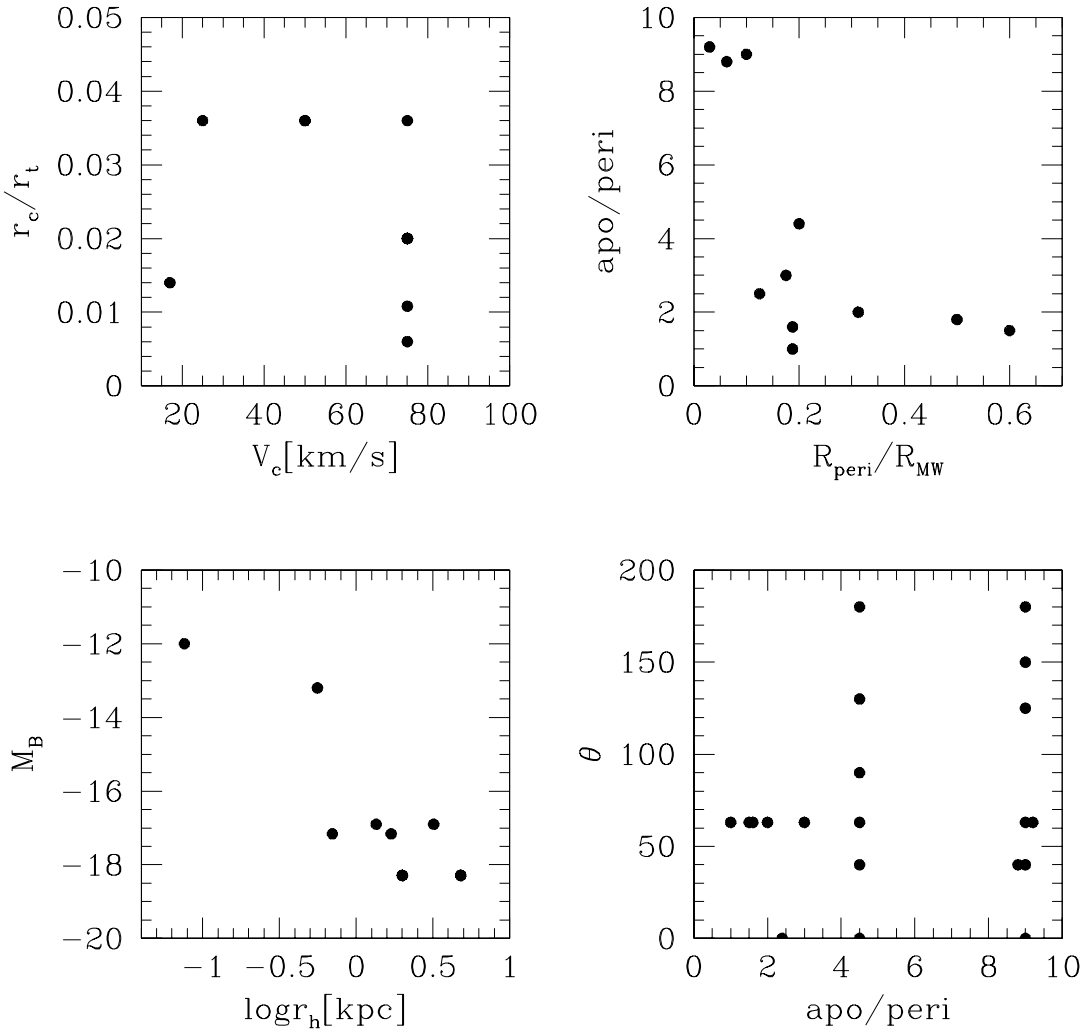

FIG. 6.—Scatter plots showing the parameter space covered by the simulations in terms of initial halo structure (the concentration r_t/r_c vs. the circular velocity V_c, *top left*), initial disk structure (the *B*-band absolute magnitude, calculated assuming $(M/L)_{*B} = 2$ as described in the text vs. the disk scale length r_h, *bottom left*), initial orbital eccentricity (apo/peri) vs. the ratio of the pericenter distance R_{peri} with respect to the virial radius of the Milky Way, R_{MW} (*top right*) and initial disk/orbit inclination (angle θ) vs. orbital eccentricity (*bottom right*). See Tables 1, 2 and 3 for details on the models and on the runs performed.

two longest principal axes of the remnant (see also Raha et al. 1991; Merritt & Sellwood 1994). The buckling gradually erases the bar symmetry, ultimately leading to a more isotropic, spheroidal configuration. The transition is highlighted by the evolution of both σ_z and the minor/major axis ratio of the stellar mass distribution, c/a (Figs. 10 and 11). The tidally induced bar and bending modes grow on the dynamical timescale once excited and thus the morphological transition is faster in high-redshift satellites, which reach a spheroidal configuration $\sim$1 Gyr after the bar appears while LSB satellites remain in a transitory, barlike configuration for a few Gyr.

After $\sim$7 Gyr of evolution, nearly all the disks have been transformed into spheroidals (Fig. 12). Heating induced by bar buckling is more important than direct heating by the tidal field. Indeed, satellites inclined by 90° with respect to their orbital plane (which suffer the strongest direct tidal heating in the direction normal to the disk plane) undergo less vertical heating compared to those on a coplanar orbit (where a stronger bar is induced), as shown in Figure 10 (see legend). It is thus understood why even a very stiff object, such as the GR 8 model, that is barely stripped, is heated into a spheroidal configuration.

The joint action of loss of angular momentum and induced vertical heating determine a marked decrease of the v/σ of the bound stellar component (Fig. 11). After the morphological transformation, the satellites remain in a nearly stable dynamical state as was verified by pushing a few simulations to over 10 Gyr.

Tidal stripping is considerably reduced when satellites are on retrograde orbits, although LSBs are still significantly damaged on orbits with small pericenters. The bar forms when the satellite performs the second pericenter passage after $\sim$5 Gyr. Vertical heating is not as strong as usual and the satellite remains quite flattened. The final v/σ within R_e is $\sim$1 in all cases. Remarkably weaker tidal tails form in retrograde orbital configurations because of an antiresonant coupling between orbital and internal motions (Toomre & Toomre 1972; Barnes 1988; Springel & White 1999; Mihos et al. 1997). In brief, this is the only orbital configuration for which the original disk structure can be partially preserved.

TABLE 2

SIMULATIONS

Run	Model	R_{peri} (kpc)	R_{apo} (kpc)	θ (deg.)
L01.....	LM1	40	360	0
L02.....	LM1	80	360	0
L03.....	LM1	40	360	180
L04.....	LM1	40	360	40
L05.....	LM1	40	360	63
L06.....	LM1	80	360	63
L07.....	LM1	40	360	125
L08.....	LM1	40	360	150
L09.....	LM1	240	360	63
L10.....	LM2	40	360	0
L11.....	LM2	80	360	0
L12.....	LM2	80	360	180
L13.....	LM2	40	360	40
L14.....	LM2	40	360	63
L15.....	LM2	80	360	90
L16.....	LM2	40	360	130
L17.....	LM2	125	250	63
L18.....	LM2	200	360	90
L19.....	LM1	75	120	63
L20.....	LM1	75	75	63
L21.....	LM1rc03	80	360	0
L22.....	LMH	80	360	0
L23.....	LM1Q4	80	360	0
L24.....	LM1 (minimal Milky Way potential)	25	220	40
L25.....	LM1 (Miyamoto disk included)	40	360	40
L26.....	LMg2	40	360	40

NOTE.—Initial conditions of the runs. We indicate the galaxy model used, the pericenter distance R_{peri}, the apocenter distance R_{apo}, and the angle between the spin of the disk and the orbital angular momentum (θ).

4.2. *Gasdynamic Simulations*

We perform two dissipational runs placing models LMg2 and HMg2 on orbits with apo/peri = 9 (runs L27 and H14 in Table 2). Figure 13 shows two important results: the gas is either stripped or funneled to the center of the galaxy. The gas loses angular momentum after the first pericentric passage, because of the torquing by the stellar bar, which is misaligned with respect to the gas (Heller & Shlosmann 1994; Mihos et al. 1997). In the HSB, only $\sim$10% of the initial gas mass is tidally stripped, while all the rest is driven to the center soon after the first pericentric passage. As a result, a central spike appears in the gas density profile (the maximum density increases by more than 2 orders of magnitude, as seen in Fig. 14), and then the profile evolves little for the following Gyr. Instead, in the LSB more than half of the gas is stripped while the remaining part is still funneled toward the center but at a slower pace, with the density growing by only 1 order of magnitude (Fig. 14).

Stripping dominates in the LSB because the gaseous disk is more loosely bound (initial gas profiles follow the stellar density profile in our models) and the central inflow is moderate as a result of both the weak bar and the long dynamical time. In the LSB, as the gas slowly drifts inward, it has time to feel the effect of tidal compression at the second pericenter passage, which leads to the largest increase in the central gas density (Fig. 14). Tidal compression occurs at the inversion points of the orbit because the direction of the tidal force relative to orbital motion is reversed. The leading front of the galaxy is thus pushed toward the trailing front. The compression will be larger at pericenters because there the magnitude of the tidal force is greater.

TABLE 3

SIMULATIONS

Run	Model	R_{peri} (kpc)	R_{apo} (kpc)	θ (deg.)
LZ1	LZ	40	360	0
LZ2	LZ	80	360	0
LZ3	LZ	40	360	180
LZ4	LZ	40	360	40
LZ5	LZ	40	360	63
LZ6	LZ	40	360	125
LZ7	LZ	75	120	63
LZ8	LZ2	70	210	63
H01.....	HM1	40	360	0
H02.....	HM1	80	360	0
H03.....	HM1	40	360	180
H04.....	HM1	40	360	40
H05.....	HM1	40	360	63
H06.....	HM1	40	360	125
H07.....	HM1	40	360	150
H08.....	HM2	40	360	40
H09.....	HM2	125	250	40
H10.....	HM2	75	120	63
H11.....	HM1rc03	50	120	0
H12.....	HMg2	40	360	40
HZ1	HMz	40	360	0
HZ2	HMz	40	360	180
HZ3	HMz	40	360	40
HZ4	HMz	40	360	63
HZ5	HMz	40	360	125
GR81.....	GR8	40	360	63
GR82.....	GR8	12	110	63

NOTE.—Initial conditions of the runs. We indicate the galaxy model used, the pericenter distance R_{peri}, the apocenter distance R_{apo}, and the angle between the spin of the disk and the orbital angular momentum (θ).

5. STRUCTURE OF THE REMNANTS

5.1. *Sizes and Density Profiles of the Stellar Remnants*

The final stellar surface brightness profiles do not deviate substantially from the initial exponential form, although they tend to become steeper (Figs. 15 and 16). In general, when the galaxy is structurally stiff or the pericenter distance is rather large ($R_{peri} > 70$–80 kpc), the profile is bimodal, having a steeper slope inside the half-mass radius R_e of the galaxy (see Figs. 15 and 16). This is because the bar instability leads to a more concentrated stellar component, which persists unless the subsequent tidal shocks are strong enough to strip the system down to the central part. As a result, both single exponential and bimodal profiles are present among LSB satellites, while stiffer HSBs or high-redshift dwarf models, in particular GR 8, are always rather stable to tides within the bar radius and thus are characterized by a bimodal profile.

The central concentration of the remnants can be measured by the distribution of their final half-mass radius R_e (Fig. 17). The higher compactness of the remnants of HSBs versus those of LSBs resembles an analogous difference seen in dEs versus dSphs (Ferguson & Binggeli 1994; Kent 1987; Carter & Sadler 1990). At the end, HSBs have a central surface brightness only slightly smaller than the initial one (even including fading), while their stellar mass is decreased by a factor of 3 or more. Therefore, they turn out to have a surface brightness higher than any dIrr with similar luminosity, just as is typically observed for dEs in the Local

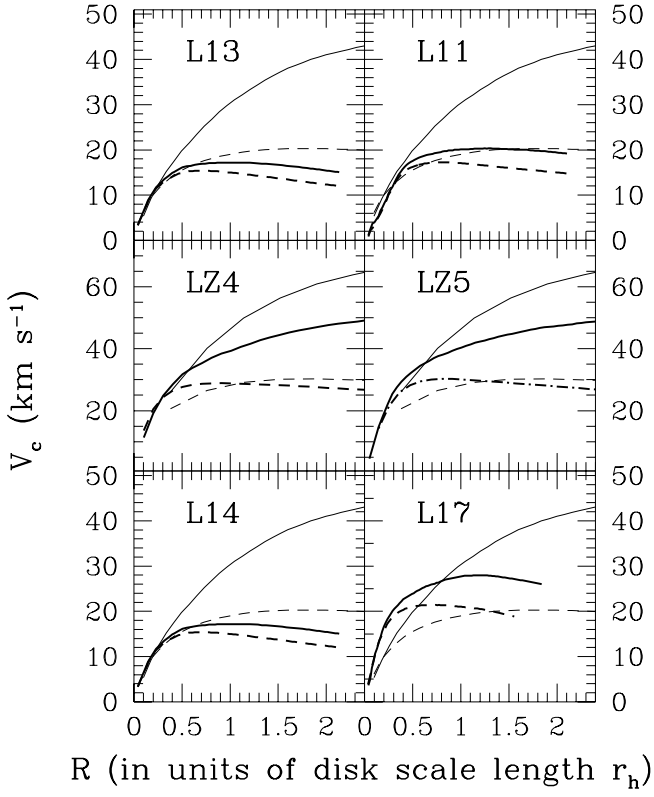

FIG. 7.—Evolution of circular velocity profiles of LSB satellites on various orbital configurations, labeled with the run names (refer to Tables 2 and 3 for details). Thin and thick solid lines are, respectively, the initial and final overall rotation curve, while thin and thick dashed lines represent the separate contribution of stars. It clearly appears that mass loss is less efficient in runs with LZ models.

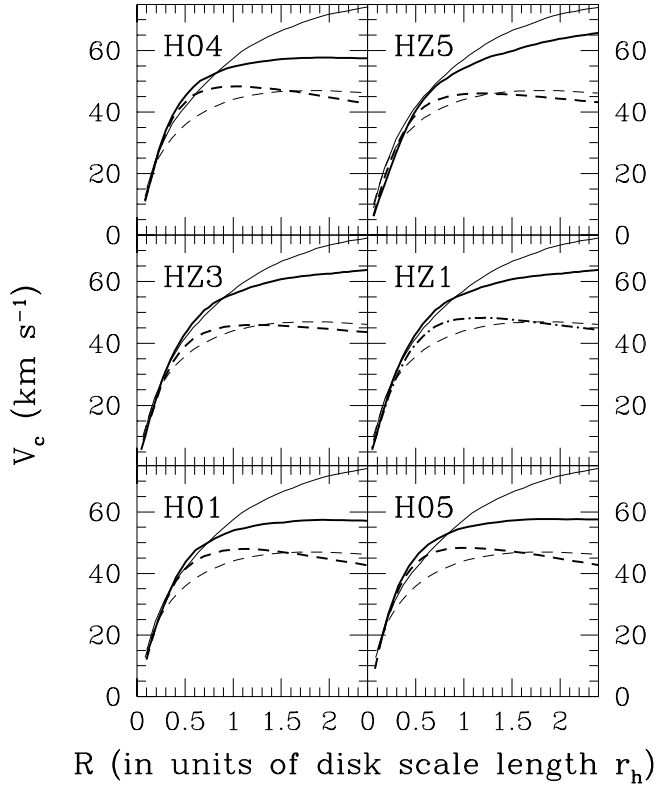

FIG. 8.—Evolution of circular velocity profiles of HSB satellites on various orbits, labeled with the run names (refer to Table 3 for details). Thin and thick solid lines are, respectively, the initial and final overall rotation curve, while thin and thick dashed lines represent the separate contribution of stars. Tidal mass loss is less efficient in HZ runs.

Group and in nearby groups and clusters (Mateo 1998; James 1991).

When fitting the profile, for some of the LSBs a single exponential law works pretty well, while King profiles with a concentration $c < 1$ reproduce better the bimodal profiles of the remnants of HSBs and of GR 8 (see Fig. 18). Because of the greater compactness of HSB remnants, their core radii in fits with King profiles are typically as small ($\sim$200–300 pc) as those of LSB remnants 10 times less massive. This well matches the observations: bright dEs like NGC 147 and NGC 185 have core radii as small as those of dSphs like Carina and Leo I (Mateo 1998), the latter being fainter by $\sim$4 mag.

In the dissipative runs, some dynamical feedback of the gas on the stellar component occurs. The latter is different in HSBs versus LSBs owing to the different dynamical evolution of their gas component. The strong central gas concentration that appears in the HSBs soon after the first pericentric passage immediately produces a response of the stellar potential and the final surface brightness profile is remarkably steeper in the center compared to the collisionless case, as is shown in Fig. 19. Instead, in the LSB, the stellar density profiles evolve nearly in the same way with and without gas because the weaker bar does not create a dense central gas knot and a substantial fraction of the gas is stripped away. The gas-to-stellar mass ratio inside $\sim R_e$ is roughly the same as at the beginning.

5.2. *Kinematics and Shapes*

The kinematics of the satellites has drastically changed by

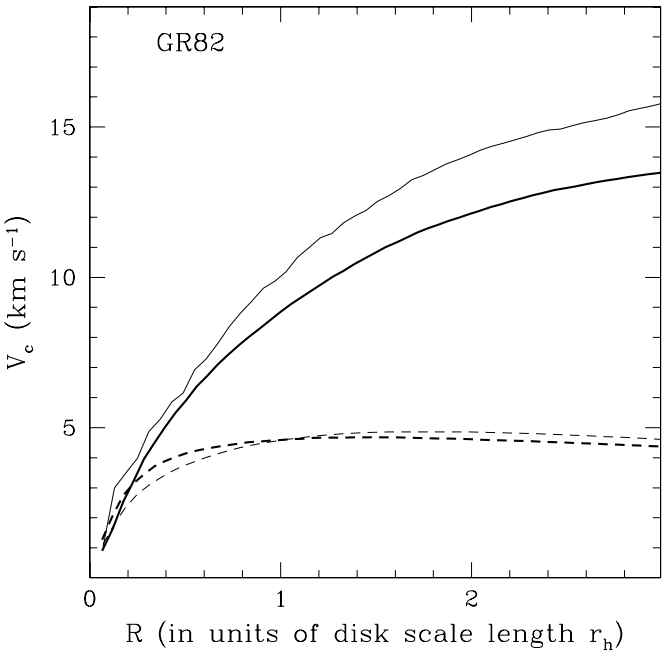

FIG. 9.—Evolution of circular velocity profile of the GR 8 model in run GR82 (see Table 3). Thin and thick solid lines are, respectively, the initial and final overall rotation curve, while thin and thick dashed lines represent the separate contribution of stars.

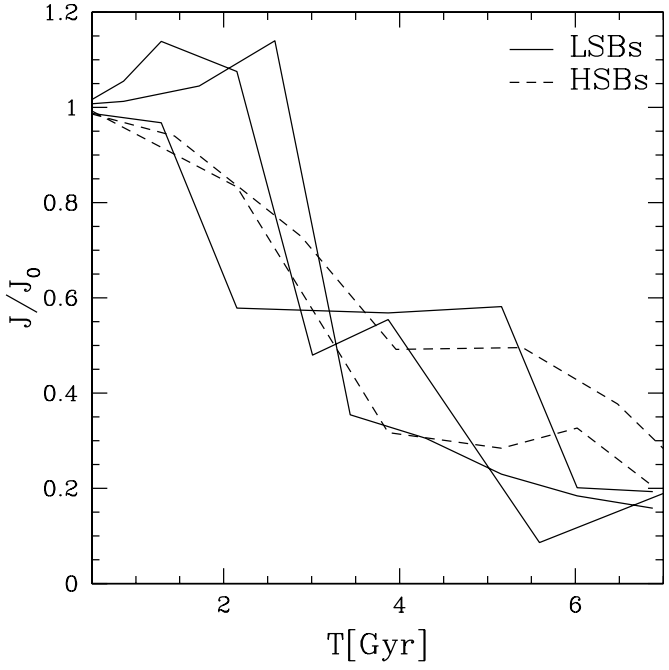

FIG. 10*a*

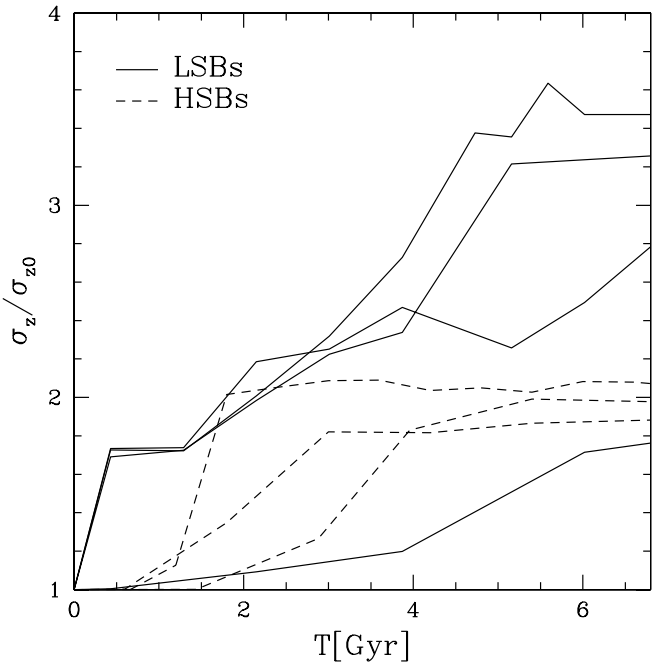

FIG. 10*b*

FIG. 10.—Evolution of the specific angular momentum is shown in (*a*), and that of the velocity dispersion normal to the disk plane, σ_z, is shown in (*b*). Both are normalized to their initial value. Results are from various runs (*dashed lines* are used for HSB satellites; *solid lines* for LSB satellites). Measurements were done within $\sim 1.5r_h$, which corresponds to the typical size of the remnants. Note that the solid line in the lower part of the plot of σ_z corresponds to run L15 (see Table 1), in which the disk is initially inclined by 90° with respect to the orbital plane, while in all other cases the inclination is $\leq 65°$.

the end of the simulations. The final v/σ measured inside R_e is typically lower than 0.5, this being a distinctive feature of dSphs and dEs not only in the Local Group but even in galaxy clusters (Mateo 1998; Bender & Nieto 1990; Bender et al. 1992; Ferguson & Binggeli 1994). A slightly larger (by 20%–30%) residual rotation is present at larger radii and is caused by high angular momentum, loosely bound material which is about to be tidally ejected.

The transition in the dwarfs' kinematics is the major success of our model as it provides an explanation for the most important dynamical difference between dIrrs and dSphs, namely, their angular momentum content. The bulk

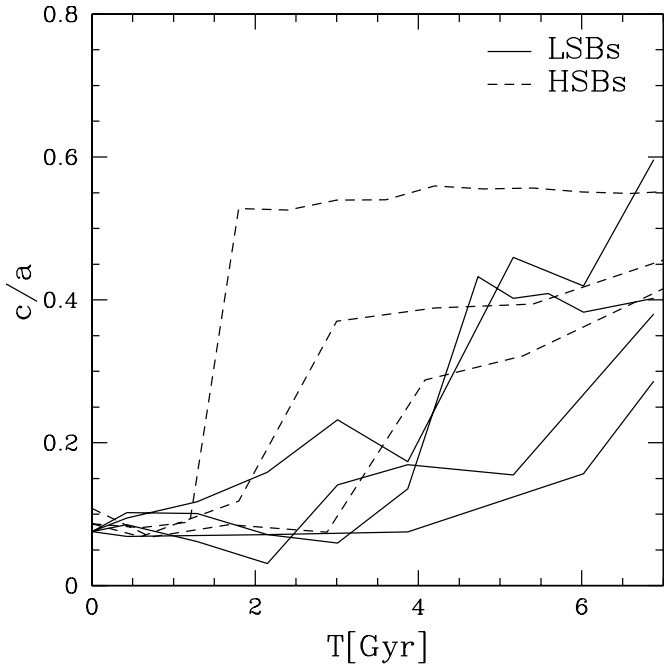

FIG. 11*a*

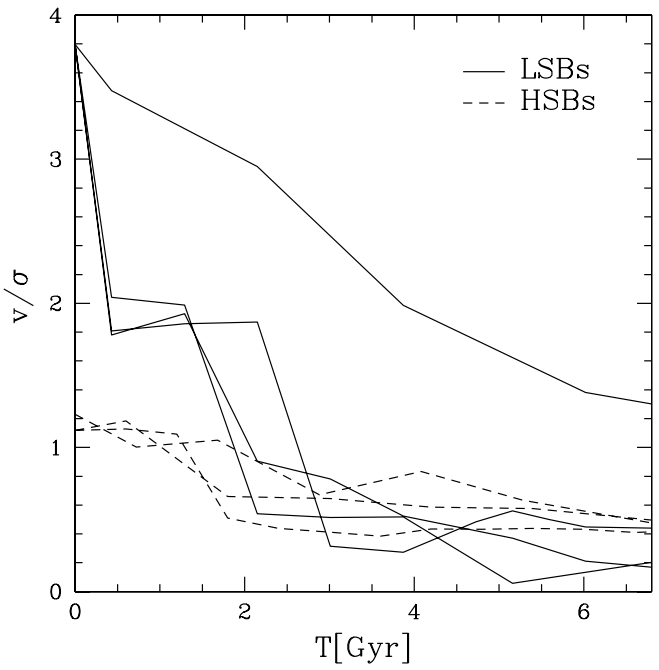

FIG. 11*b*

FIG. 11.—Evolution of the minor/major axis ratio of the bound stellar component is shown in (*a*), and that of v/σ is shown in (*b*). Results are from various runs (*dashed lines* are used for HSB satellites; *solid lines* for LSB satellites) and were made within $\sim 1.5r_h$, which corresponds to the typical size of the remnants.

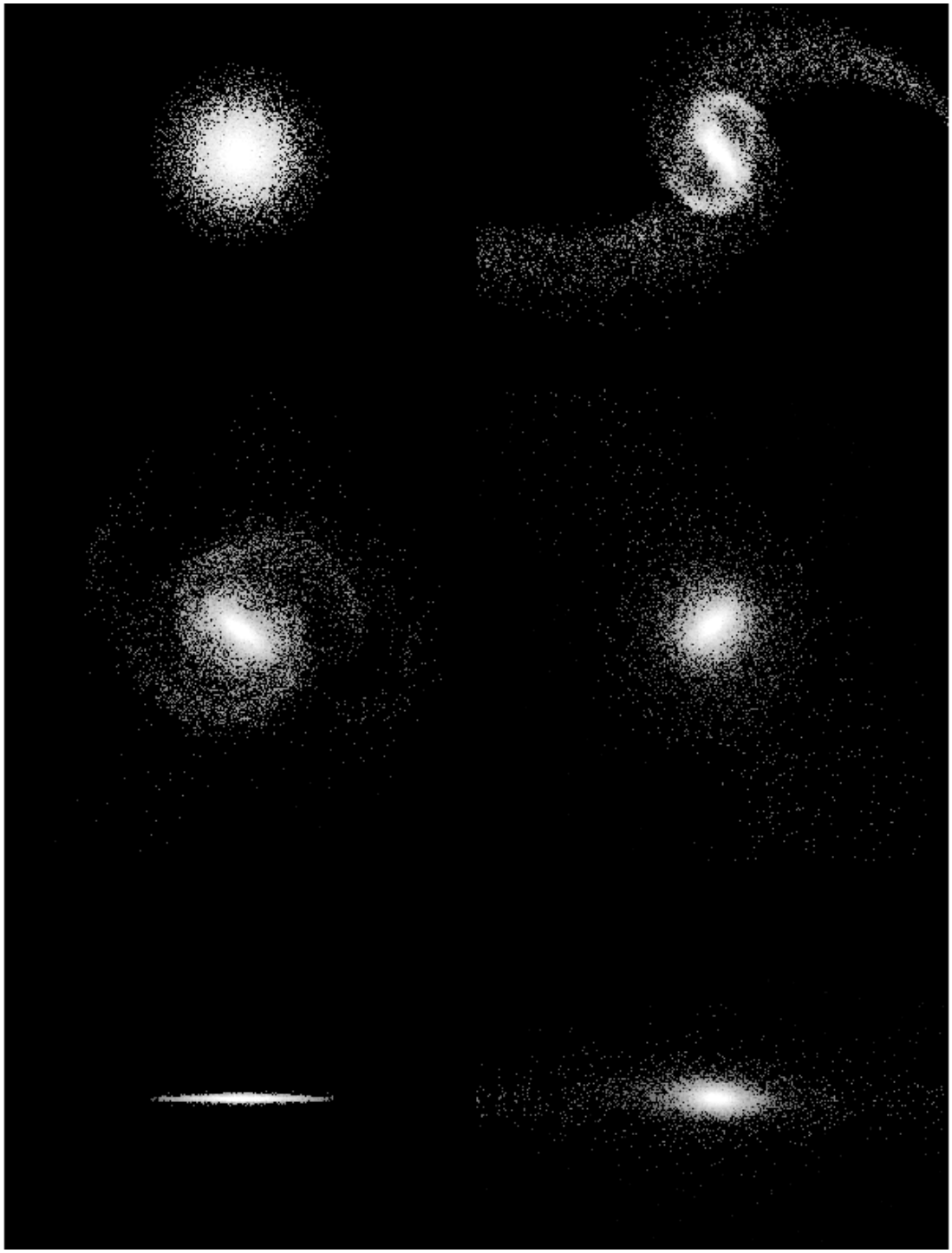

FIG. 12.—Evolution of an HSB dwarf disk galaxy inside a Milky Way–sized halo (run H01). Color-coded logarithmic density plots of the stellar component of the satellite—the darker the color, the lower the density—are shown. Boxes are about 30 kpc on each side. *From top to bottom:* The first four snapshots show a face-on projection of the satellite at every 2 Gyr starting from $t = 0$ (*top left*) and moving clockwise; the two bottom snapshots show the initial (*left*) and final (*right*) appearance of the disk seen edge on.

of the result is independent from the viewing projection, as can be seen in Figure 20, which shows that all the remnants fall below the theoretical prediction for rotationally flattened spheroidals, $v/\sigma \sim (\epsilon/1 - \epsilon)^{1/2}$, where $\epsilon = 1 - b/a$ is the ellipticity projected onto the plane of the sky (see Binney & Tremaine 1987).

The final average velocity dispersions vary from 10 to 20 km s^{-1} among LSB remnants, while they are around 30–35 km s^{-1} for those of HSBs (Fig. 21). The initial models of LSBs and HSBs span exactly the same range of masses and both have initial velocity dispersions of a few km s^{-1} (only $\sim 30\%$ larger in the HSBs), being rotationally supported. It is the larger mass retained by the HSB satellites together with their typically more concentrated final stellar profile that determines such a kinematical distinction. The velocity dispersions of the remnants of LSBs are in good agreement with those inferred for dSphs, while those of the remnants of HSB match those of dEs (Mateo 1998). Tidal forces do not

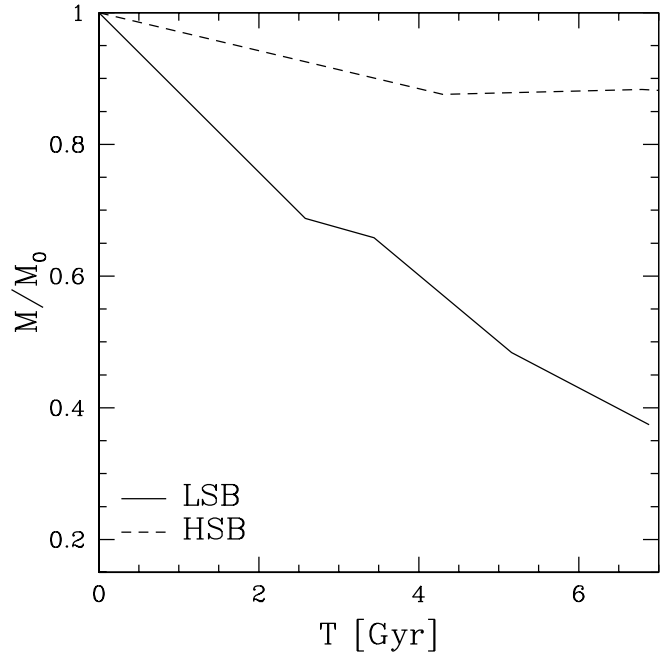

FIG. 13*a*

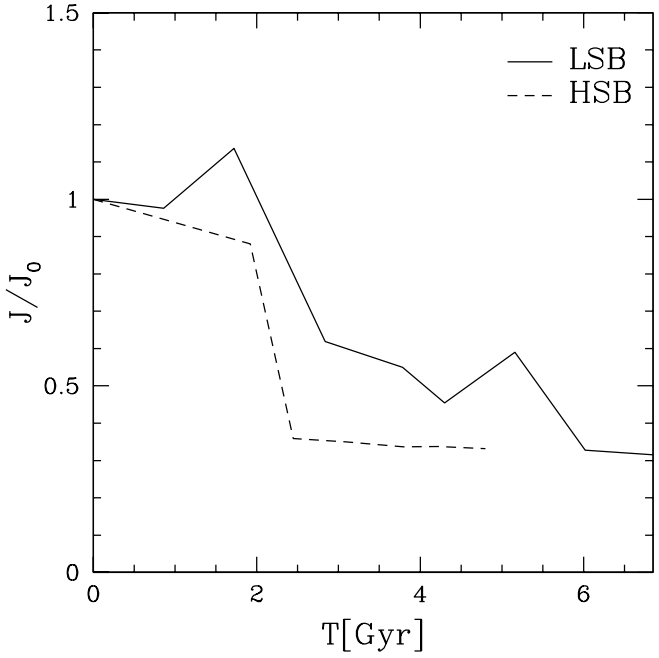

FIG. 13*b*

FIG. 13.—Evolution of the bound gas mass (*a*) and of the specific angular momentum of the gas (*b*) for the LSB (*solid line*) and for the HSB satellite (*dashed line*).

significantly inflate the central velocity dispersions beyond that expected from virial equilibrium. This is in agreement with Piatek & Pryor (1995) and Pryor (1994), who performed a similar analysis on spherical satellites; a nearly virialized stellar core survives in our simulations, notwithstanding the strong shocks suffered on the most eccentric orbits (but see § 6.2 for the few cases in which the disruption can take place). The central density of our models, which is a critical parameter in determining the response to a given tidal perturbation, would have been much lower if we had not included dark matter; therefore, it is not surprising that the purely stellar systems in Kuhn & Miller (1989) and Klessen & Kroupa (1998) dissolve very easily when exposed to Galactic tides. Furthermore, a lower density system would have a lower characteristic frequency, closer to the orbital frequency, which again would favor complete disruption by resonances (we already discussed a similar concept in regard to the different response to tides of LSBs and HSBs—see § 4.1). However, even in our simulations, the observed kinematics can be different from the intrinsic ones

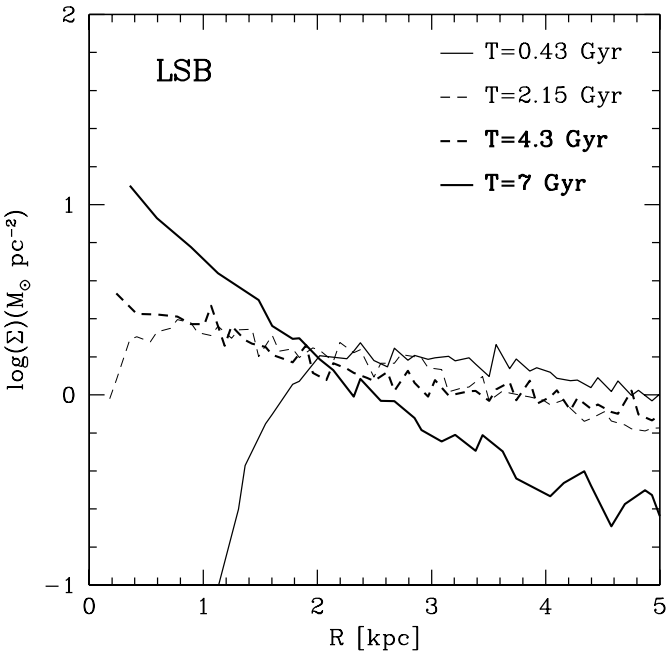

FIG. 14*a*

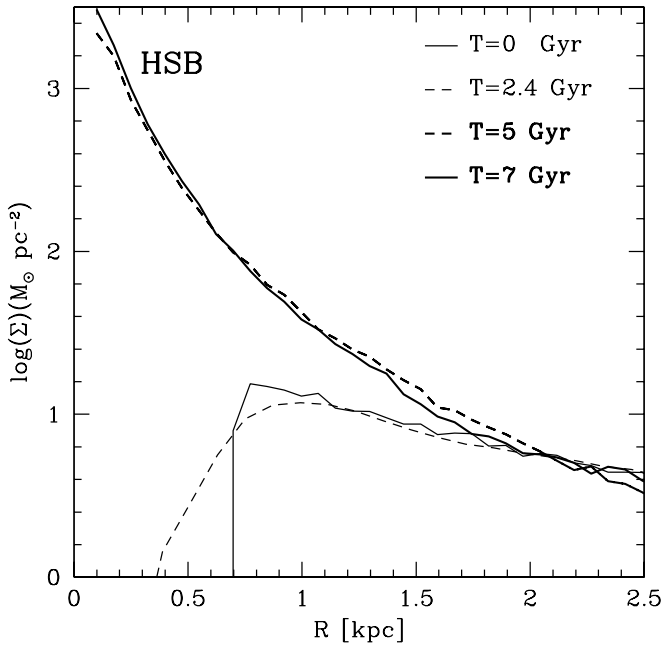

FIG. 14*b*

FIG. 14.—Evolution of the gas surface density in the LSB satellite (*a*) and in the HSB satellite (*b*)

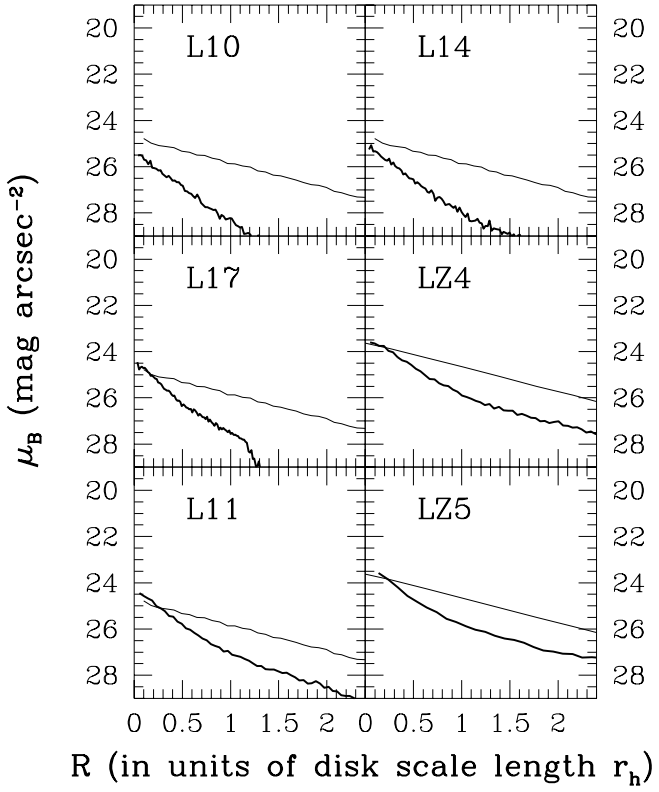

FIG. 15.—Evolution of the surface brightness profiles of LSB satellites: the thin line is used the initial profile; the thick line is used the final profile. The various panels are labeled with the run names (see Tables 2 and 3 for details). Normalization of the final profiles takes into account the fading of the stars as derived in § 9.

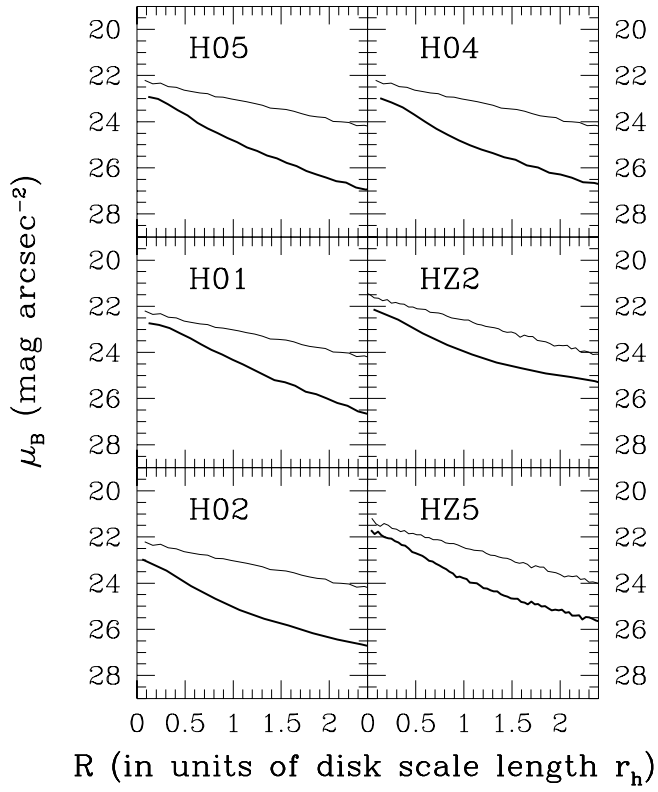

FIG. 16.—Evolution of the surface brightness profiles of HSB satellites: the thin line is used for the initial profile; the thick line is used for the final profile. The various panels are labeled with the run names (see Table 3 for details). Normalization of the final profiles takes into account the fading of the stars as derived in § 9.

because of the projection effects caused by the unbound stars that surround the remnant (see § 5.4).

The velocity dispersion profiles of the remnants are typically slowly decreasing (Fig. 22), as is found in some of the dSphs (Hargreaves et al. 1994a, 1994b, 1996) and dEs (NGC 205, Held et al. 1990, 1992; Carter & Sadler 1990).

The fact that rotation is negligible in the remnants means that any substantial flattening will be caused by anisotropy of the velocity dispersion, similar to that of giant ellipticals and different from that of low-luminosity ellipticals (Ferguson & Binggeli 1994). The final radial velocity anisotropy, measured by the parameter $\beta = 1 - \sigma_z/\sigma_p$, is higher in the more flattened LSBs (Fig. 23). The average value of β is $\sim$0.15 for HSBs and 0.35 for LSBs. Thus, remnants are on average only mildly anisotropic.

To measure the shape of the remnants, we use the triaxiality parameter $T_t = (a^2 - b^2/a^2 - c^2)$ (Franx, Illingworth, & de Zeeuw 1991), where a, b, and c are, respectively, the major, intermediate, and minor axis of the remnants. $T_t = 1$ represents a purely prolate halo, while we have $T_t = 0$ for a purely oblate halo. Objects can be defined as nearly prolate if $\frac{2}{3} < T_t < 1$, nearly oblate if $0 < T_t < \frac{1}{3}$, and triaxial if $\frac{1}{3} < T_t < \frac{2}{3}$. In measuring the shape of the remnants within R_e, we find that the majority of the remnants are nearly prolate spheroidals and a fair fraction are triaxial, while oblate shapes are really rare. The tendency toward prolateness is caused by the residual radial anisotropy originated during the bar stage of the evolution and can be enhanced by tidal distortion, especially for the loosely bound LSBs.

The parameter c/a provides a measure of the maximum observable flattening of the remnants: the higher the flattening, the lower will be c/a. Figure 23 clearly indicates that the remnants of LSBs are more flattened than those of

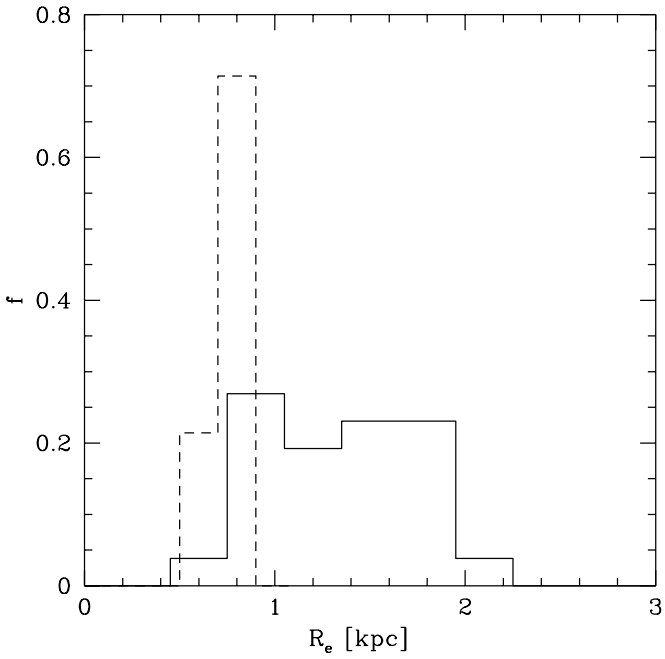

FIG. 17.—Histogram showing the fraction of the remnants, f, for which the half-mass radius falls within the values indicated on the x-axis, for both LSBs (*solid line*) and HSBs (*dashed line*).

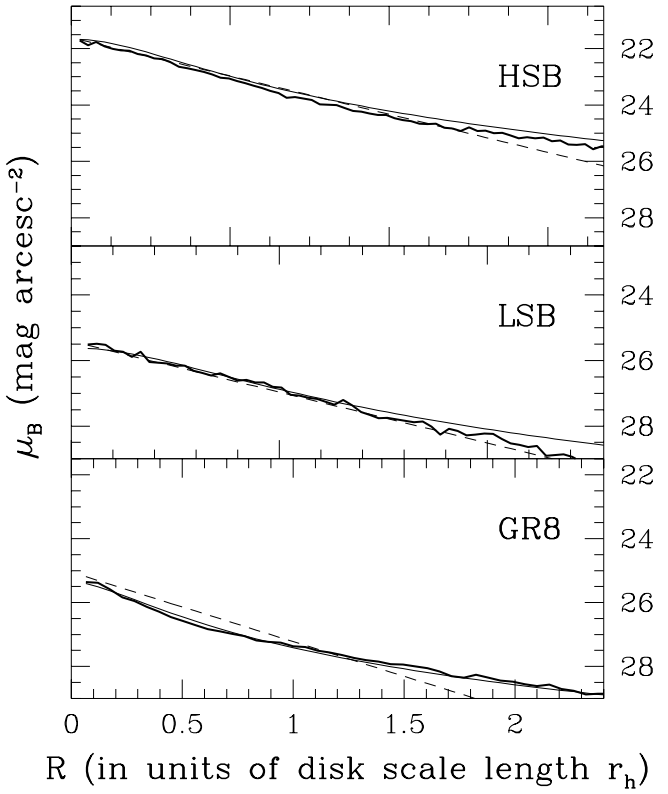

FIG. 18.—Final surface brightness profiles of "prototype" satellites (*thick solid lines*) fitted by exponential laws (*thin dashed lines*) or King profiles (*thin solid lines*). Exponential scale lengths used are 400 pc (HSB, run H08), 1 kpc (LSB, run L10), and 50 pc (GR 8, run GR82), while the core radii in the fits with King profiles are 325 pc (HSB), 800 pc (LSB), and 50 pc (GR 8).

HSBs, with average c/a of 0.35 and 0.5, respectively. This is expected given the different strength of instabilities in HSBs versus LSBs. The more flattened remnants correspond to cases of nearly retrograde encounters that better preserve the original disk structure.

An anticorrelation between final surface brightness and final flattening is present in the remnants. Interestingly, there are indications that bright dEs, both in the Local Group and in galaxy clusters, are rounder than low surface brightness dSphs (van den Bergh 1996; Ferguson & Sandage 1991). However, the comparison with observations is not trivial because we have to take into account projection effects. For example, if viewed along the major axis, all the remnants would appear rounder than when viewed along either of the two other axes, as seen in Figure 23. The mean ratio between two of the principal axes, obtained averaging over the three projections, is thus higher than that associated with the measure of c/a, being around 0.5 for the remnants of LSBs and around 0.7 for the remnants of HSBs. We can consider the latter values as yielding the mean observable flattening.

Ellipticities of LG dSphs range from the extreme value of 0.8 in Sagittarius and 0.65 for Ursa Minor to 0.2–0.3 for Sextans, with the average being around 0.4 (Mateo 1998). We can safely conclude that the ellipticities of the remnants fall in the observed range.

When the gas is included in the model satellites, we observe an increase in the final rotation of the stars inside R_e, by $\sim 30\%$ in the LSB and by about 50% in the HSB. The reason is that the gas spins up the stellar bar while losing angular momentum (Friedli 1999; Friedli & Benz 1993). This mechanism is suggested by Figure 24, in which we compare the evolution of the specific angular momen-

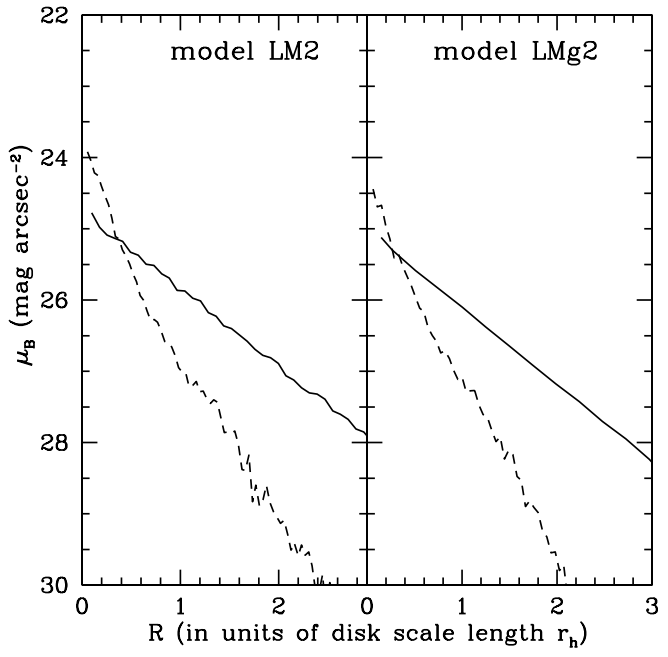

FIG. 19*a*

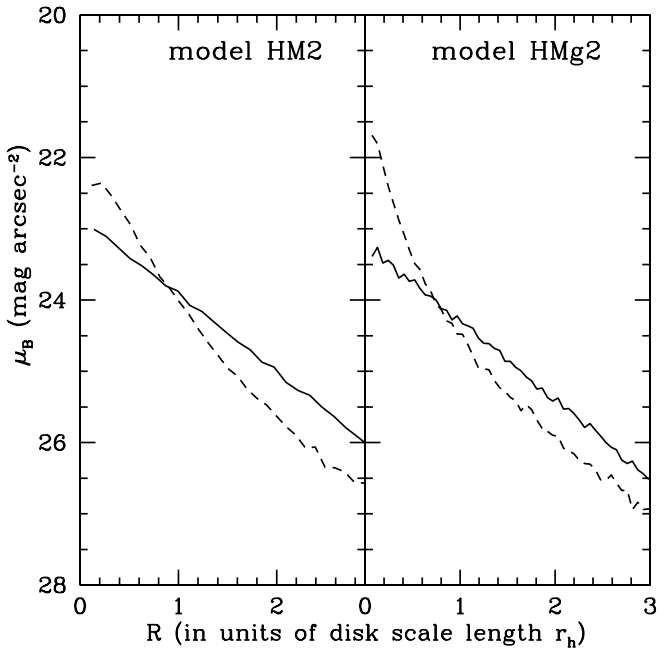

FIG. 19*b*

FIG. 19.—Comparison of the final surface brightness profiles (with no fading correction) for the satellites with gas (*right panels*) and without gas (*left panels*). Orbital configurations are exactly the same in all four runs (the collisionless runs are L13 and H08; see Tables 2 and 3). In (*a*) the LSBs are shown, in (*b*) the HSBs. Solid lines refer to the profiles at $T = 0$, dashed lines to those after 7 Gyr. Note that the initial surface brightness profiles are not exactly the same in collisionless and dissipational runs, the effective stellar surface density being lower because a part of the same total disk mass is assigned to the gas component in the latter case.

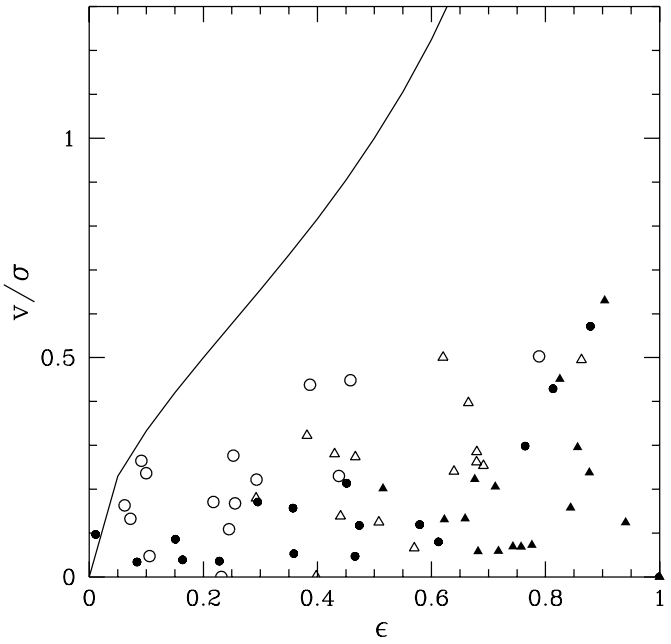

FIG. 20.—Scatter plot showing the relation between final v/σ and projected ellipticity (see text), both measured inside R_e, for LSBs (*filled symbols*) and HSBs (*open symbols*) for two viewing projections, one along the intermediate axis (*circles*) and the other along the major axis (*triangles*) of the remnants (rotation perpendicular to the minor axis is always close to zero, thus results for the viewing projection along the latter axis are not shown). The solid line shows the relation expected for rotationally flattened spheroidals (Binney & Tremaine 1987).

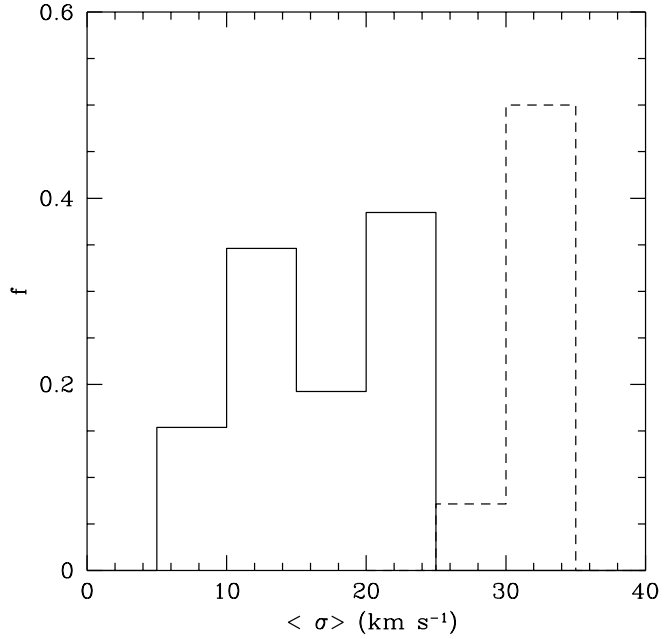

FIG. 21.—Histogram showing the fraction of the remnants, f, for which the average velocity dispersion falls within the values indicated on the x-axis: the solid line refers to the stellar remnants of LSBs; the dashed line is for the stellar remnants of HSBs.

tum of the bound stellar component with and without gas. Because rotation is higher, the remnant of the LSB is also flatter ($c/a = 0.32$ instead of 0.48) than in the collisionless case. In the case of the HSB, the dominant effect is instead the stronger central concentration of both the gas and the stellar components and thus the remnant is rounder, notwithstanding the higher rotation ($c/a = 0.67$ instead of $c/a = 0.55$). Overall, the final v/σ increases slightly for the LSB while it is almost unvaried for the HSB because a higher velocity dispersion is achieved given the more concentrated potential. A rounder shape of gaseous remnants was also found by Moore et al. (1998) for harassment in galaxy clusters as, in that case, the model galaxies were all of the HSB type.

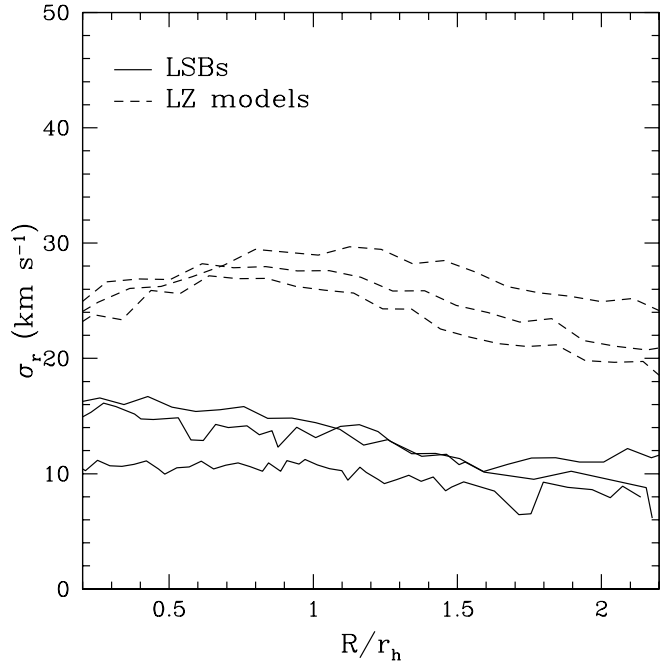

FIG. 22*a*

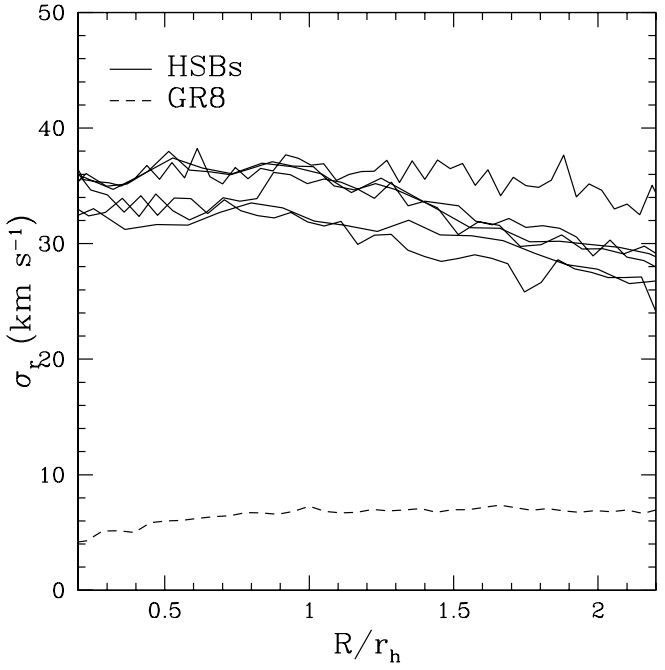

FIG. 22*b*

FIG. 22.—Radial velocity dispersion profiles of LSB remnants (in (*a*), the dashed lines are for LZ runs) and HSB remnants (in (*b*), along with the profile for the GR 8 model, represented by the dashed line).

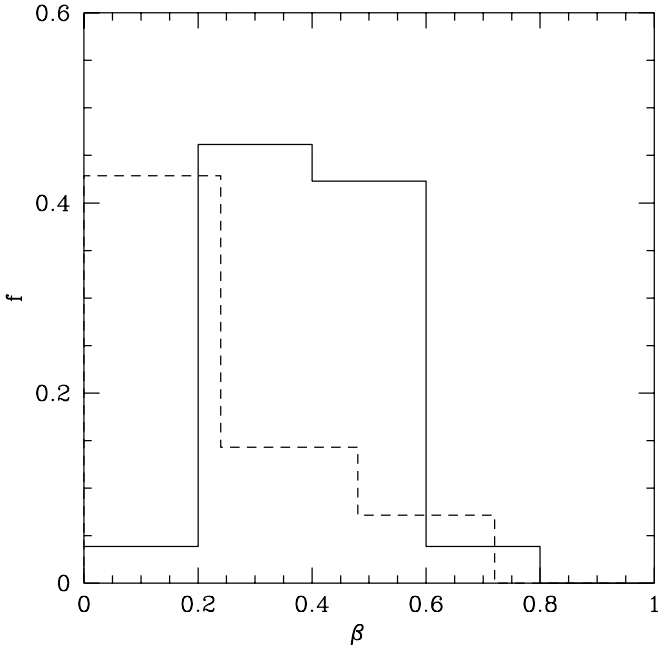

FIG. 23*a*

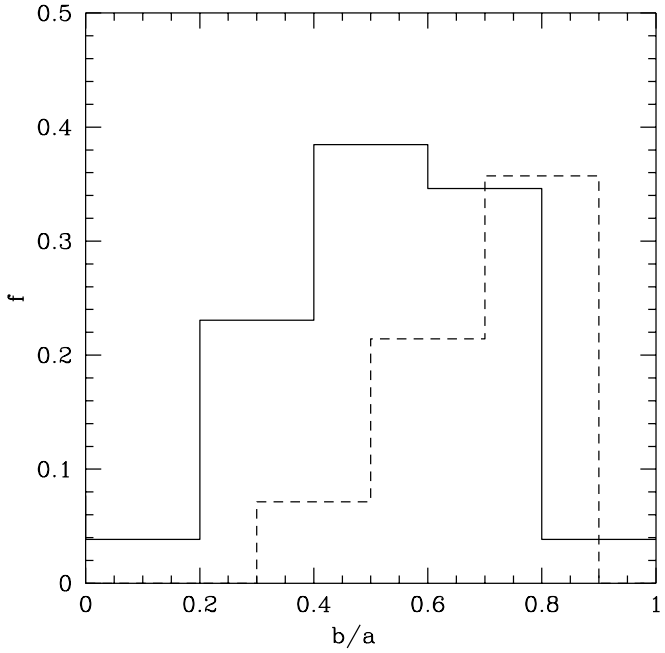

FIG. 23*b*

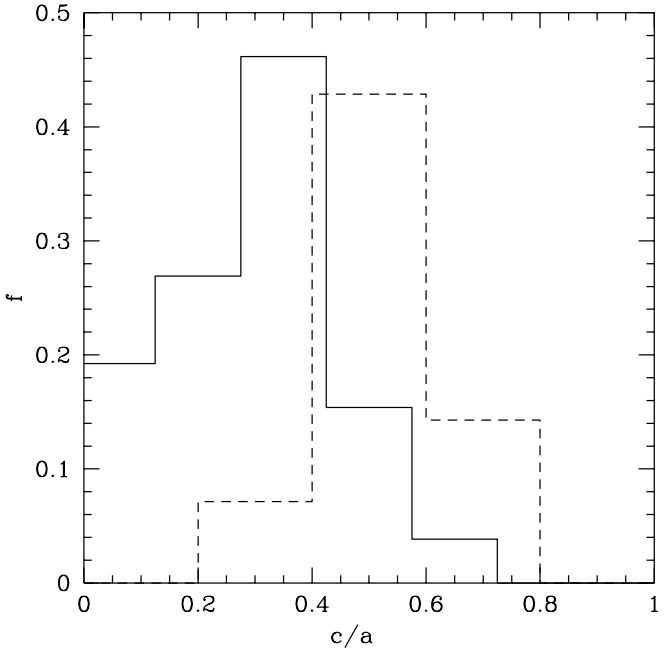

FIG. 23*c*

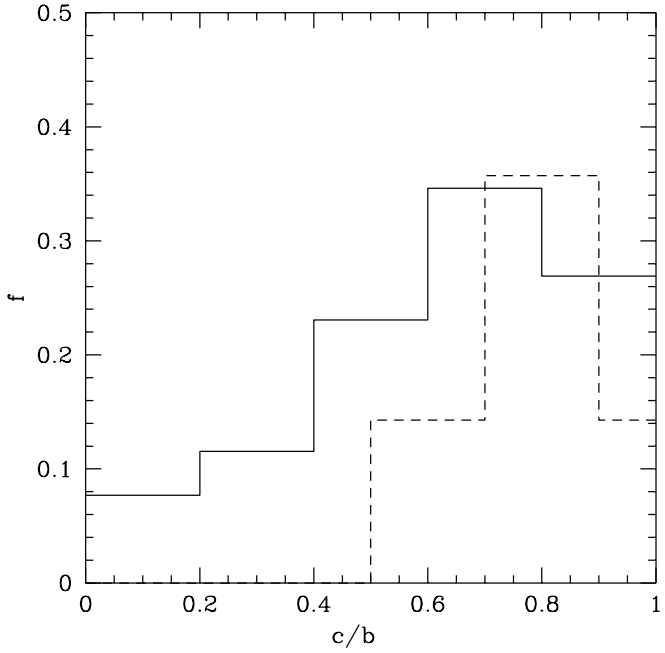

FIG. 23*d*

FIG. 23.—Histograms showing the fraction of the remnants, *f*, for which the anisotropy parameter β (*a*) or apparent ellipticities resulting from the ratios of two of their principal axes (plots b, c, and d) fall within the values indicated on the *x*-axis: the solid line is for the remnants of LSBs; the dashed line is for the remnants of HSBs.

5.3. *Dark Matter Content*

The circular velocity profiles (Figs. 7, 8, and 9) show the relative contribution of dark matter and stars after 7 Gyr of evolution inside the Milky Way potential. Remnants of LSBs, being severely stripped down to their inner parts, have a "central" $M_{\rm dark}/M_{\rm stars}$ (measured inside R_e) around 1–2, while their high-redshift counterparts (LZ models) can have ratios as high as 4–5. HSBs, although quite resistant to tides, have in general $M_{\rm dark}/M_{\rm stars} \sim 2.5$ as they start off with a ratio $M_{\rm dark}/M_{\rm stars}$ (within the optical radius) a factor of 2 lower than that in LSB models.

Contrary to common belief, not all dSphs have extremely high dark matter contents. Most of them have inferred central mass-to-light ratios (measured at the core radius) between 5 and 20 (Mateo 1998), which, for the stellar mass-to-light ratios expected in objects dominated by old stars $[(M/L)_{*B} \geq 3]$, implies dark matter halo masses within the range of our results. Mass-to-light ratios in dEs turn out to be moderate, ≤ 10 (Carter & Sadler 1990), in agreement with those of the remnants of HSBs.

Our evolutionary model is able to explain also the extreme dark matter content of the faintest dSphs, Draco,

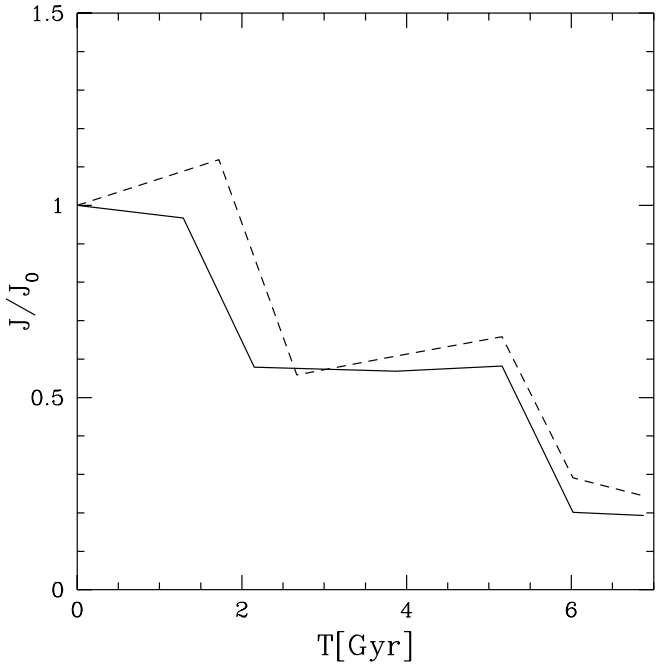

FIG. 24*a*

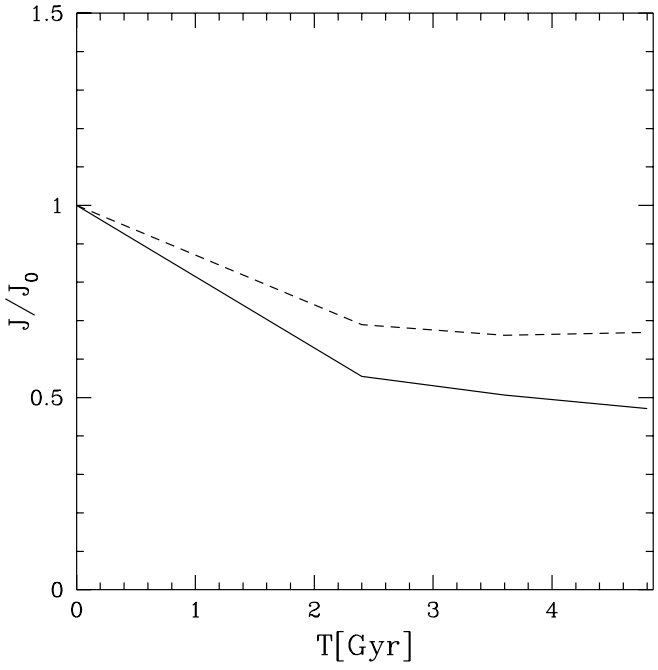

FIG. 24*b*

FIG. 24.—Evolution of the specific angular momentum of the bound stellar component in collisionless (*solid line*) vs. dissipational (*dashed line*) runs. In (*a*) results for an LSB run are shown, while in (*b*) we plot those relative to an HSB run. Orbital parameters are those of runs L13 (LSBs) and H08 (HSBs), listed in Tables 2 and 3.

and Ursa Minor (Lake 1990; Hargreaves et al. 1994a, 1994b; Mateo 1998). The GR 8–like model almost preserves the initial $M_{\rm dark}/M_{\rm stars}$: with $M_{\rm dark}/M_{\rm stars} \sim 12$ within R_e, the mass-to-light ratios would be ≥ 36 for $(M/L)_{*B} \geq 3$.

A dwarf as dense as GR 8 needs to enter early in the Milky Way halo to be transformed into a dSph, requiring a high number of tidal shocks and thus a small orbital time. The hierarchical structure formation scenario naturally meets these conditions because the densest objects form, on average, earlier and are accreted by the main halos on orbits with smaller radii (see § 3). We have shown that the transformation occurs on a orbit with apocenter ~ 100 kpc, in agreement with the present distances of Draco and Ursa Minor (Mateo 1998). As time goes on, lower density dwarfs will form and enter an enlarged Milky Way halo. These will be on wider orbits and will be likely similar to the standard LSB models, thus ending up in dSphs with lower mass-to-light ratios. A correlation between distance and mass-to-light ratio should thus arise and indeed is suggested by observations (Mateo 1998; Irwin & Hatzidimitriou 1995).

Early-type dwarf galaxies in the Local Group show a certain spread in their total central densities (including baryons and dark matter; see Mateo 1998). Comparing these data with the densities of our remnants shows a remarkably good agreement. The final central densities of the remnants of LBS are as low as those of most dSphs (e.g., Sextans, Sagittarius, and Fornax), i.e., $0.01 < \rho_0 < 0.1\ M_\odot\ {\rm pc}^{-3}$ (Mateo 1998). The remnant of GR 8 is comparable to the densest dSphs, Draco, Sculptor, and Ursa Minor, having $\rho_0 > 0.1\ M_\odot\ {\rm pc}^{-3}$ (Lake 1990). Even higher densities are reached in the inner part of the remnants of HSBs thanks to the highly concentrated stellar potential, as found in dEs. However, central densities as high as those of NGC 205 ($\rho_0 \sim 5\ M_\odot\ {\rm pc}^{-3}$; see Mateo 1998) appear only in the gasdynamic runs (model HM2g), in which the profile of the stellar component steepens remarkably.

It is important to note that the postinteraction spread is only slightly larger than that of the initial models. Therefore, our ability to reproduce the vast range of properties of dSphs results from the choice of initial models spanning a range of central densities. The spread in the concentration c in the initial models is a factor of 4, which corresponds to a factor of almost 20 in the initial central densities ($\rho \sim c^2$ for truncated isothermal spheres). In cold dark matter models, the typical concentration of halos on a scale $M \lesssim 10^{10}\ M_\odot$ is as high as that of our GR 8 model. Cosmological N-body simulations show that the scatter of the concentration at a given mass scale is large (Bullock et al. 2001) but no as much as to encompass the extremely low values associated with our LSB models. Interestingly, the latter values seem to be very common for small halos formed in warm dark matter (WDM) cosmogonies (Bode, Ostriker, & Turok 2001; Eke, Navarro, & Steinmetz 2001).

5.4. *Tidal Effects and the Measure of M/L*

The issue of the high mass-to-light ratios found in some of the dSphs is critical for understanding in general the nature of dark matter (Lake 1990). Many authors have pointed out that some steps of the core fitting procedure used to derive M/L for dSphs and/or tidal effects could lead to overestimations of them (Piatek & Pryor 1995; Irwin & Hatzidimitriou 1995; Kuhn & Miller 1989; Klessen & Kroupa 1998).

It is usually assumed that mass follows light in dSphs. In Figure 25, we see the comparison between final total mass and stellar mass profiles for three "prototype" models. For HSB and LSB remnants, one would actually slightly underestimate M/L (by 10%–30%) by assuming that mass follows

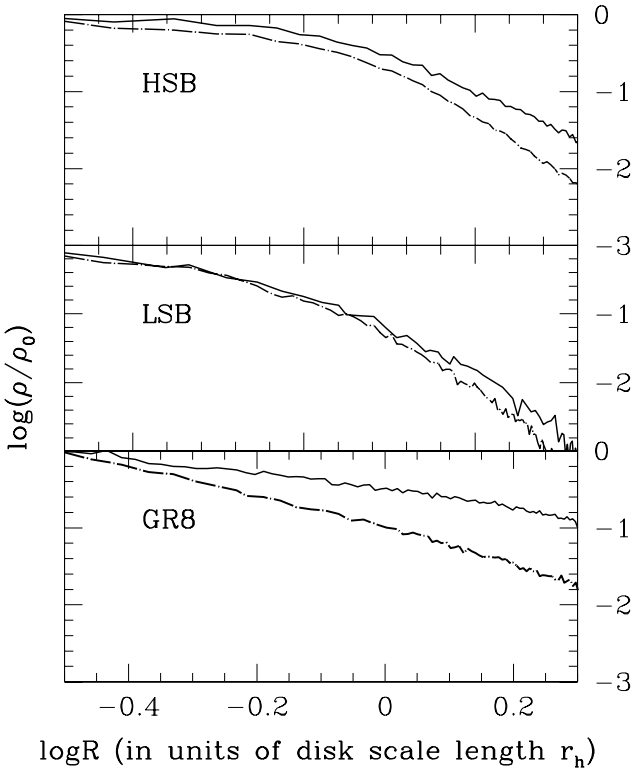

FIG. 25.—Comparison between final total mass (*solid line*) and stellar mass profiles (*dot-dashed line*) for various remnants inside the final tidal radius (the corresponding runs are H08, L10, and GR82). Densities are normalized to their central values.

light. The difference is instead remarkable for models as stiff as GR 8, where we would underestimate the dark matter mass by a factor ~ 2.

We can also ask whether the assumptions that (1) the measured velocity dispersion can be interpreted as resulting from virial equilibrium and that (2) such equilibrium is an isotropic hold for our remnants.

Almost all of our remnants have reached a nearly stable equilibrium by the end of the simulations. However, in some of them, a fair degree of rotation is present in addition to the velocity dispersion, and this should be taken into account when estimating the virial mass of the object. In a few cases, in which $v/\sigma \geq 0.5$, one would underestimate the true mass-to-light ratio by nearly a factor of 2 considering only the contribution of the velocity dispersion to the kinetic energy (because $M \sim \langle v^2 \rangle$). Therefore, if, for example, Ursa Minor has substantial rotation (Armandroff, Olszewski, & Pryor 1995; Hargreaves et al. 1994a), the true M/L could be even higher than usually estimated. According to Figure 23, the maximum value of the anisotropy parameter β is ~ 0.8, which means that velocity dispersion in the plane of the galaxy can be a factor ~ 2 higher than that normal to the plane (here we are assuming that the velocity dispersions along the two principal axes lying *within* the plane are comparable, as is found in most of the remnants). At most, one would overestimate the one-dimensional velocity dispersion by only $\sim 20\%$ (from $\sigma_{1d} = [(\sigma_x^2 + \sigma_y^2 + \sigma_z^2)/3]^{1/2}$), which leads to an overestimate of a factor $\lesssim 1.4$ for M/L (from $\Delta\sigma^2 \sim \Delta M$) as upper limit. However, only $\lesssim 5\%$ of the remnants exhibit such high final radial anisotropies.

A more interesting possibility is provided by tidal effects: the measures of line-of-sight velocity dispersion (and thus the M/L) could be overestimated if the unbound, fast-moving stars making up tidal tails are included by chance in spectroscopic samples; the latter tend to produce a rising velocity dispersion profile as a result of the velocity gradient associated with the gradual mass loss. The tails extend to several kpc from the center of the dwarf. If the mass loss is high (comparable to the bound mass), and if the line of sight of the observer falls close to one of the tails, the contami-

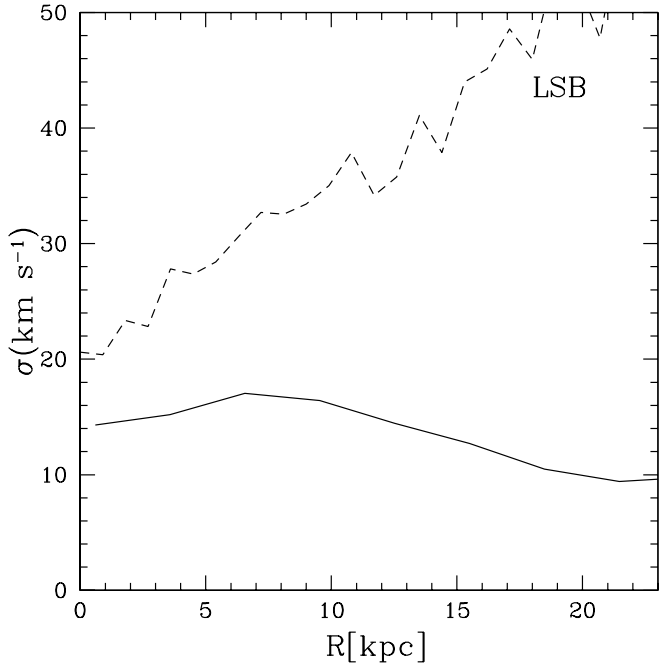

FIG. 26*a*

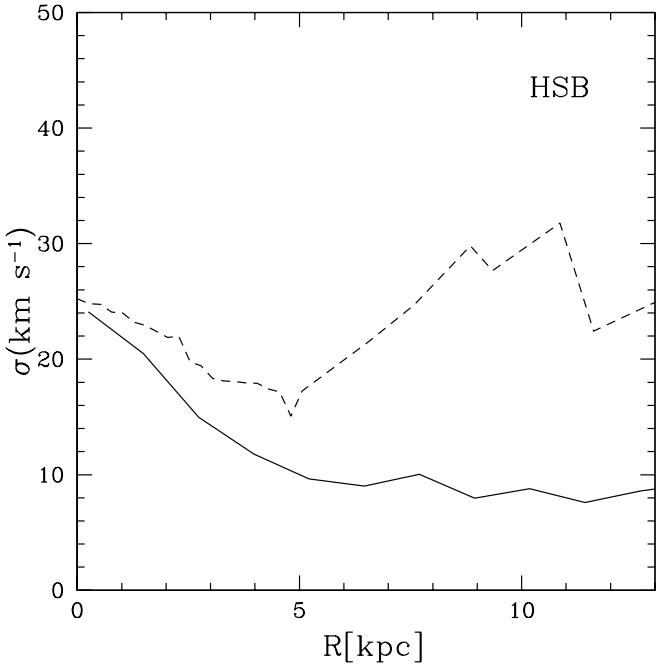

FIG. 26*b*

FIG. 26.—Intrinsic velocity dispersion (*solid line*) and apparent velocity dispersion when the line of sight is along one of the tidal tails (*dashed line*) for both an LSB (*top*) and an HSB remnant (*bottom*). The runs have the same orbital parameters (runs L10 and H08).

nation by unbound stars could show up even at small projected distances from the center.

This is illustrated in Figure 26, where we show the results for both LSBs and HSBs on a direct orbit (run L10 and H08, see Table 2); these yield an upper limit to the bias in the velocity dispersion profiles as any other orbital configuration would produce weaker tails. In these extreme cases, we find that the central velocity dispersion can be overestimated by as much as $\sim 40\%$ for the LSB, while for the HSB the difference is only a few percent. As a consequence, the mass-to-light ratio can be overestimated by a factor $\lesssim 2$ in the case of the LSBs while it is unchanged with respect to the true value for the HSBs (the latter statement obviously applies even to denser dwarfs, such as the GR 8 model). The remarkable difference in the projected velocity dispersion profiles of LSBs versus HSBs is simply a result of the very different tidal mass losses.

If the orbits of the dwarfs are quite eccentric, as suggested by simulations of structure formation (Ghigna et al. 1998), the probability that one of the tidal tails points close to the line of sight of an observer located at the center of the orbit will be high (our displacement with respect to the Galactic center is negligible given the large distances of most dSphs). A velocity dispersion that increases outside the core of the dwarf should be considered as a warning of a possible contamination by tidal tails; on the other end, kinematical samples of the central area could contain so many unbound stars that it might be difficult to discard them and identify the bound population. Using more than one statistical tool to remove the outliers can certainly alleviate the problem (Cote et al. 1999). However, we conclude that tidal effects cannot rule out the need of high dark matter contents in some of the dSphs: objects such as Draco and Ursa Minor ($M/L > 25$) would still have $M/L > 12$, even with the maximum velocity dispersion enhancement just described. The velocity gradient associated to the tidal tails could explain the origin of the rotation apparently detected in some dSphs (e.g., Ursa Minor in Hargreaves et al. 1994b and Armandroff et al. 1995).

6. THE NATURE OF TIDAL STIRRING: THE DEPENDENCE ON INITIAL CONDITIONS

So far we have based our description of the numerical results on the set of satellite models that we consider more akin to typical observed dIrrs and we have placed them on the typical orbits found in N-body simulations of structure formation. Furthermore, we have considered only one form of the primary potential, the global parameters for which were fixed again based on structure formation models. To figure out how general the "tidal stirring" mechanism explored in this paper is, in this section we will relax each of these hypotheses, one at a time, investigating a much wider parameter space.

6.1. *Dependence on the Initial Structure of Satellites*

As mentioned in § 2.1, we have built a special set of models that should be the least prone to bar and/or bending instabilities by varying Q, the initial disk thickness or the core radius of the halo (see Table 1 for the models' parameters and Fig. 2 for the intrinsic stability properties).

We mostly placed such models on a direct orbit with moderate eccentricity (apo/peri = 4, $R_{\rm peri} = 80$ kpc): this configuration, in which the excited bar is barely damaged by tidal stripping even in the case of the fragile LSBs, is ideal for studying the vertical heating caused by bar-buckling. The results are illustrated in Figure 27. An LSB model with a small core radius (run L21) undergoes a smaller increase of σ_z (by about $\sim 50\%$) compared to the standard reference case (run L02). A weaker bar develops because the higher halo central density damps the unstable modes and the buckling is then reduced because of the lower radial anisotropy. An analogous result is obtained with an HSB disk embedded in a more compact halo (model HM1rc03), which has an initial rotation curve very similar to that recently derived by Sofue (1999) for the LMC. If placed on a nearly circular orbit (run H11) as implied by recent astrometric measurements (Kroupa & Bastian 1997), the kinematics remain disklike at $R > R_e$ (stripping is very modest), but a thick spheroidal component develops after 5 Gyr. These results qualitatively agree with those obtained by Weinberg (2000) in a detailed study of the response of the LMC to the tidal field of the Milky Way. The thick spheroid could be responsible for some of the microlensing events seen toward the LMC (Evans & Kerins 2000). In models with $Q = 4$ (run L23), namely, those that are considerably "hotter" than the standard models, the bar is also weak and σ_z increases by less than a factor of 2.

We then explore models with a larger scale height ($z_s = 0.3 r_h$) and $Q = 2$ (model LMH in run L22): the vertical dispersion increases by only 40%, a factor ~ 3 less than in run L02. This is not surprising because in this model σ_z is initially 2 times larger than usual, placing the dwarf well above the critical radial anisotropy level necessary for the onset of bending (see Raha et al. 1991).

Despite the different degree of evolution reported in these "peculiar models," the final v/σ inside the half-mass radius is always less than 1, with the exception of run L22. However, the latter case is rather unrealistic as late-type

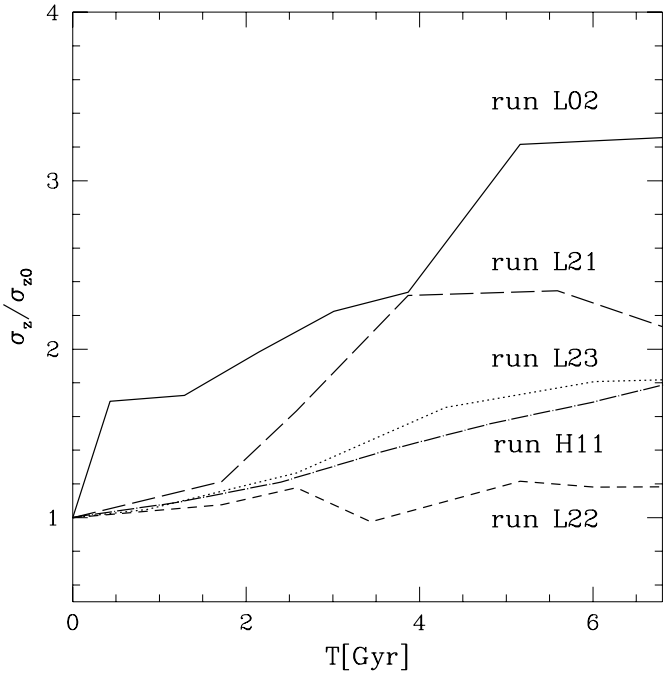

FIG. 27.—Variation of the vertical velocity dispersion with respect to the initial value in runs using models with different intrinsic stability properties (see Tables 2, 3, and 1 for the full description of, respectively, the runs and the satellite models employed).

spiral and dwarf irregular galaxies show a tendency toward very thin disks (see Van der Kruit & de Grijs 1999).

In general, our evolutionary model seems quite robust: tidal shocks are too strong for the initial stability properties of the models to change substantially the final outcome of tidal stirring.

6.2. *Dependence on the Orbital Parameters*

In this section we will investigate the extent to which the effectiveness of tidal stirring is related to the orbital parameters and, in particular, to the eccentricity of the orbits. Although eccentric orbits are expected for satellites in the framework of hierarchical structure formation (Ghigna et al. 1998), so far observational data have been more in favor of nearly circular orbits (e.g., Schweitzer et al. 1995). We thus perform a number of runs in which satellite models are placed on low-eccentricity orbits. LSB satellites on orbits with apo/peri ~ 1.5 maintain $v/\sigma > 1$ and a disklike appearance even after 7–8 Gyr if their pericenters are larger than 150 kpc (run L08 and L17), irrespective of the disk/orbit orientation. On the other end, if the orbits have equally low eccentricity but considerably smaller pericenter, both LSBs and HSBs do transmute into a spheroidal galaxy (run L16 and H09) after a few orbits. In the latter case, the apocenter ($R_{\rm apo} \sim 250$ kpc) is comparable to the present distance of the farthest dSph, Leo I, and more and stronger tidal shocks are suffered by the satellite because orbital times are shorter (~ 3 instead of 5 Gyr) and pericenters are nearly almost a factor of 2 smaller.

However, compared to the standard runs employing high-eccentricity orbits (e.g., run L1–L15 and H01–H08), the velocity at pericenter is sensibly lower (~ 280 instead of 400 km s^{-1}); therefore, the encounter takes place in a "less impulsive" regime. Consequently, the satellite should respond more adiabatically to the perturbation. Evidently, the lower velocity is not able to counterbalance the effect of the large perturbing mass of the Milky Way halo when the pericenter distance is sufficiently small. Therefore, orbital energy (or pericenter distance) is at least as important as orbital eccentricity in setting the effect of tides, as was found also by Gnedin et al. (1999) using an analytical approach.

From our wide exploration of parameter space, we can deduce that the orbital time $T_{\rm orb}$ is the most significant parameter and that tidal stirring has been effective within the past 10 Gyr only for satellites having $T_{\rm orb} \leq 4$ Gyr, which corresponds to a circular orbit with a radius $\lesssim 0.5R_{\rm vp}$ ($R_{\rm vp}$ being the virial radius of the Milky Way).

Very dense satellites require smaller orbital times, which allows them *more and stronger shocks* (a smaller orbital time implies a smaller $t_{\rm enc}$—see § 4.1), as is shown by the simulations of GR 8. In the framework of hierarchical structure formation, this comes out automatically as, on average, they formed earlier and fell into the Milky Way halo when it had a smaller virial radius. Thanks to the rescaling properties of halos (see § 2), the condition on the orbital time is automatically generalized for every redshift z if we assume that $R_{\rm vp}$ is the virial radius of the main halo *at the redshift of infall.*

The present distances of most of the dSphs in the Milky Way or M31 systems are within $0.5R_{\rm vp}$ (assuming $R_{\rm vp} \sim 400$ kpc) and should thus satisfy the constraint on the orbital time. However, the farthest dSph, Leo I, having a distance of about 270 kpc, probably lies at the boundary of the "allowed" region. Thus, if Leo I was tidally stirred by the Milky Way, it must be on a fairly eccentric orbit in order to have a sufficiently small orbital time despite its large apocenter distance. At more than 800 kpc from the Milky Way, the Tucana dwarf (Gallart et al. 1999) could be the greatest challenge for our model if future measurements of its internal kinematics will confirm that it is a dSph in all respects. A few satellites on nearly radial orbits with apocenters far exceeding the virial radius of the primary halo, and just inside the turnaround radius, are indeed found in N-body simulations (Ghigna et al. 1998).

We also performed a few runs to explore the regime of *very tightly bound orbits*, namely, those with a corresponding circular radius $\leq 0.3R_{\rm vp}$. In particular, we consider the case of nearly circular and circular orbits with apocenters less than 130 kpc (runs L19, L20, LZ7, H10). Orbits of this type would be consistent with the present distances of some of the Milky way satellites, the LMC, Sculptor, Ursa Minor, Draco, and Sagittarius.

What would be the fate of a fragile LSB satellite on such orbits? Our simulations indicate that LSBs are completely disrupted on nearly circular or even exactly circular orbits at a distance of ~ 75 kpc (runs L19 and L20). The mechanism is simply one of continuous mass loss (Fig. 28). The disks of LSBs are so large that the tidal radius falls within them at these short orbital distances and, thus, they are dramatically destabilized. The system responds to strong mass loss by expanding and thus reducing even further its binding energy (Binney & Tremaine 1987; Gnedin & Ostriker 1999). The destruction is faster on a circular orbit (Fig. 28) because the orbit-averaged tidal force is stronger. This is in agreement with N-body results on the survival of cosmological halos on tightly bound orbits (Kravtsov & Klypin 1999). Instead, HSBs or LZ models (run H10 and LZ7) have disks lying inside their tidal radius and thus lose mass only after tidal heating has sufficiently loosened their potentials. They lose 20% of their stellar mass and transform into a spheroidal but survive for several Gyr.

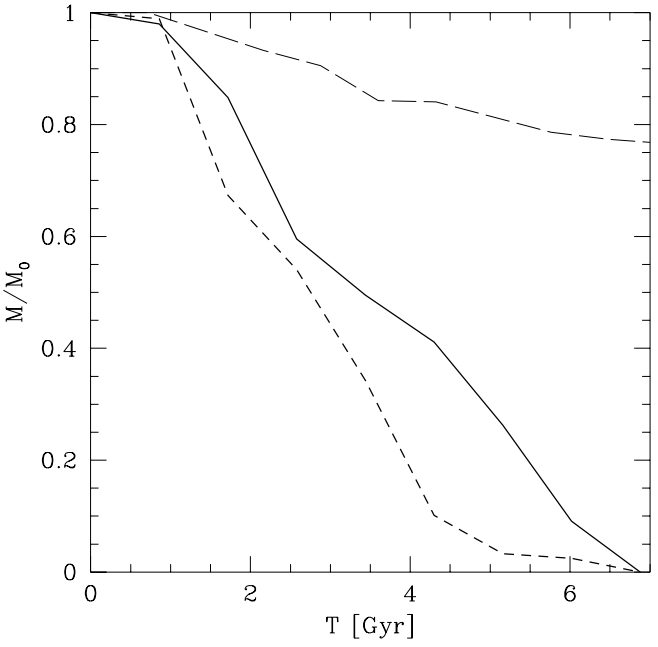

FIG. 28.—Tidal mass loss for satellites on low-eccentricity, tightly bound orbits. The long-dashed line is for an HSB (run H10), the solid line is for an LSB on the same orbit (run L18), and the short-dashed line is for an LSB on a circular orbit (run L19).

We conclude that low surface brightness satellites cannot survive too close to the Milky Way or M31; in particular, we find that they need to be on orbits such that their typical distance from the center of the primaries is greater than 70 kpc, which, interestingly, is true for most of the Local Group dSphs.

Sagittarius, which is located at a much smaller distance (<25 kpc), is likely a nearly disrupted remnant of an LSB satellite. In runs L19 and L20, a density enhancement along the streams is still recognizable for a few Gyr and has a maximum elongation $b/a = 0.2$ similar to that inferred for Sagittarius (Mateo 1998). In this extreme situation, our results converge somewhat to those obtained for purely stellar satellites by Kuhn & Miller (1989) and Klessen & Kroupa (1998).

Stable satellites at short distances from the Milky Way must have high central dark matter densities, as indeed seems to be the case for the nearby Draco and Ursa Minor dSphs (Mateo 1998; van den Bergh 1999), or they must have steep rotation curves as those of our HSB models, as in the case of the Magellanic Clouds.

6.3. *Dependence on the Primary Halo Potential*

A primary halo as massive and extended as adopted so far is expected in structure formation models and is consistent with the observed radial velocities of satellites once even the farthest of the group, Leo I and Leo II, are taken into account (Zaritsky et al. 1993; Wilkinson & Evans 2000).

To explore the influence of the Galactic halo, we placed an LSB model on a bound eccentric orbit with apocenter of 220 kpc and pericenter of 25 kpc (run L24, see Table 2) within a "minimal halo" advocated by (Little & Tremaine 1987) extending to only 50 kpc. The apocenter of this orbit is still sufficiently large to be consistent with the distance of the second most distant dSph satellite, Leo II (~200 kpc). Because of the truncation of the potential, the orbital time is larger than for orbits with similar parameters in the standard potential (~5 instead of ~3 Gyr); thus, the satellite performs only one pericenter passage in 7 Gyr. The lower number of shocks as well as the longer time spent by the dwarf far from any significant influence of the tidal field produce a remnant with a still recognizable disk structure and $v/\sigma \sim 0.8$, larger than that of any dSph. In Figure 29, we see the evolution of v/σ for this run (L24) and also a comparison with run L17 (see Table 2), the latter having a similar apocenter and an even lower eccentricity in the standard halo model. In Figure 29, we can also see that the circular velocity profile evolves much less than in the case of LSB satellites in the standard primary halo (Fig. 7), indicating that stripping is comparatively modest. These results strengthen the point made in the last section, namely, that the orbital time is the key parameter determining the transformation. Moreover, they highlight that primary halos as massive and extended as those formed in CDM cosmogonies are required to explain with tidal stirring the origin of *all* Local Group dSphs out to the distances of Leo I and Leo II.

The plunging orbits chosen in many of our simulations penetrate quite close to the center of the primary halo, at 30–40 kpc. The Milky Way and M31 have disks that extend at least to 15–20 kpc. However, their mass is expected to be small compared to that of their halos, even if they do not have $M_{\rm dark}/M_{\rm stars}$ ratios as high as those of dwarf galaxies (Persic & Salucci 1997). To test the validity of our results when the primary disk is also included, we placed an LSB satellite (the most sensible to variations in the tidal forces) on an orbit with pericenter of 40 kpc in the usual isothermal

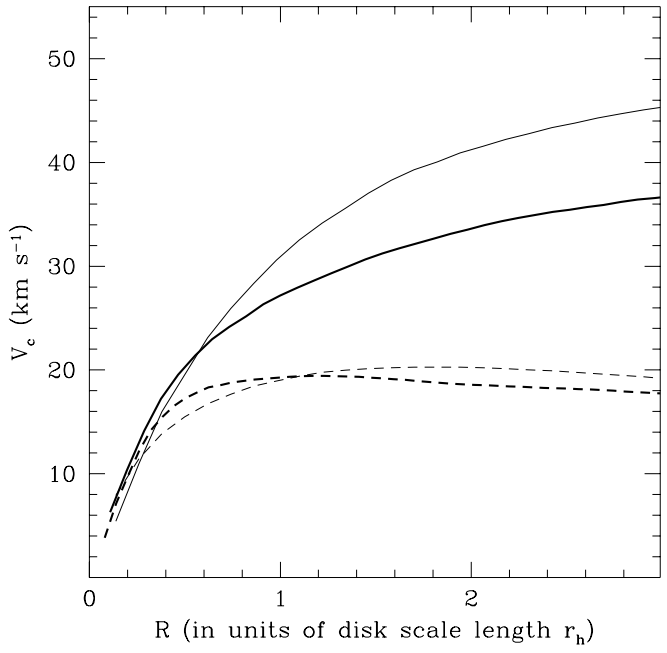

FIG. 29*a*

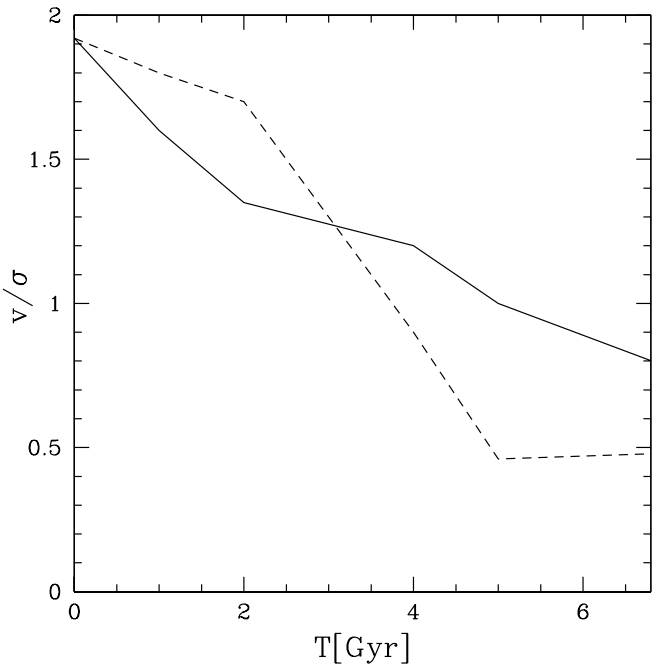

FIG. 29*b*

FIG. 29.—(*a*) Final circular velocity profile of the LSB dwarf evolved in the "minimal" Milky Way halo (see text), in run L24 (*thick lines*), plotted against the initial profile (*thin lines*). The contribution of the stellar component is represented by the dashed lines. In Fig. 7, an analogous plot for a run in which the satellite has a similar orbit in the standard Milky Way halo (run L17) is shown. (*b*) Evolution of the v/σ of the bound stellar component for run L24 (*solid line*) and for run L17 (*dashed line*), the latter using the standard model for the primary halo.

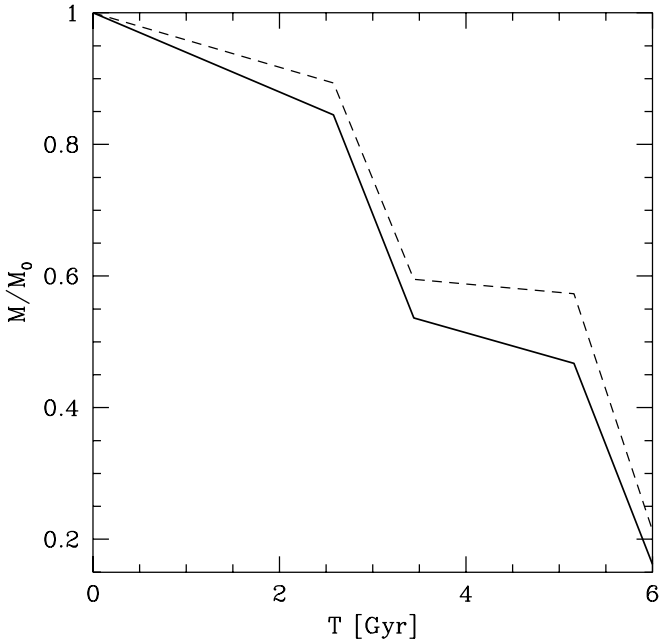

FIG. 30.—Evolution of the bound stellar mass for the LSB satellite when the disk potential is included in the primary (*solid line*, run L25) or when only the dark matter halo of the primary is responsible for the external perturbation (*dashed line*, run L13). The same orbit was used in the two runs.

halo and we added to the latter a disk with a structure similar to that of the Milky Way (i.e., with a mass 6×10^{10} $M_\odot$ and scale length of 3 kpc).

The disk was modeled using a Miyamoto-Nagai potential

$$\Phi_M(R, z) = -\frac{GM}{\sqrt{R^2 + (a + \sqrt{z^2 + b^2})^2}}, \quad (5)$$

where $R = (r^2 - z^2)^{1/2}$ is the disk radius in cylindrical coordinates, a is the scale length, and b is the scale height. We set $b/a = 2$ (Binney & Tremaine 1987). Comparing the results obtained in this run (L25) with an analogous run in the standard primary potential (L13), we see only marginal differences. As illustrated in Figure 30, the mass of the remnant after 6 Gyr is very similar, although the addition of a central disk component to the primary halo slightly enhances stripping. We thus conclude that the tidal shock is always dominated by the halo, even for quite small pericenter distances.

7. STAR FORMATION HISTORY

From the evolution of the gas surface density observed in the gasdynamic runs (§ 4.2), we can calculate the evolution of the star formation rate (SFR) of the dwarfs using the Kennicutt law (Kennicutt 1998). This is a phenomenological law, calibrated using large samples of disk galaxies, from dwarf irregulars to large spiral galaxies, and relates the *specific* star formation rate $dM_*/dtdA$ (measured in $M_\odot$ yr^{-1} kpc^{-2}) to the gas surface density Σ_g. At a given location in a galaxy, we have

$$\frac{dM_*}{dtdA} = \alpha \frac{\Sigma_g}{t_{\rm dyn}}, \quad (6)$$

where $t_{\rm dyn}$ is the dynamical time of the gas. The efficiency α is ~ 0.1 for the best fit indicated by Kennicutt (1998) using a large data set, although the same data show a large scatter, especially for faint galaxies. For nonstarburst dwarf galaxies, with SFRs (≤ 0.1 $M_\odot$ yr^{-1}), α ranges between 0.01 and 1.

We calibrate α for our model galaxies by requiring that the satellites, from their formation until the time they enter the Milky Way halo, have a constant star formation rate high enough to produce the stellar mass of our initial models (models LMg2 and HMg2; see Table 1). Therefore α may vary depending on their formation epoch. We consider two formation epochs for the dwarfs, either 12 or 15 Gyr, as the age of the oldest stars in dSphs falls within this range (Grebel 1999; Hernandéz, Gilmore, & Valls-Gabaud 2000), while we always assume that they entered the Milky Way halo 10 Gyr ago. The SFRs and related parameters are reported in the legend to Figure 31. With this procedure, the specific SFRs for LSB satellites turn out to be of the same order as those recently derived for local dIrrs such as Sextans A and GR 8 using *HST* photometry (Dohm-Palmer et al. 1997, 1998) and are quite close to those derived for isolated LSB galaxies using N-body/SPH simulations (Gerritsen & de Blok 1999). LSBs require high values of α because of the low surface density of their disks; for HSBs, the efficiencies are, instead, closer to the "best fit" given by Kennicutt (1998), which is not surprising as the galaxies in that sample are mostly normal, high-surface brightness disks.

From the time at which we start the simulations up to the final time, we compute, for each output, the specific SFR as a function of radius, calculating the values of Σ_g and $t_{\rm dyn}$ in equally spaced radial bins (in calculating Σ_g, we always take into account the gas mass that has already being consumed at the previous output in a given bin). We then calculate the average SFR in the dwarf integrating over its area (only out to $2r_h$ because the gas is rapidly stripped at larger radii) and weighting by the gas mass in each bin.

The resulting star formation histories are shown in Figure 31. In the case of the LSB, the star formation rate has a periodic behavior, with peaks of activity quite well correlated to each pericenter passage. The exact number and height of the peaks depends on the efficiency parameter α: when this is high, the gas is consumed mainly in the first two bursts and there is only a small amount left when the satellite approaches the primary for the third time. The small starbursts are separated by a timescale of ~ 3.5 Gyr, roughly the orbital time of the dwarf galaxy. Qualitatively, these star formation histories bear a striking resemblance to those recently derived for Leo I and Carina by Hernandéz et al. (2000) using *HST* color-magnitude diagrams. An analogous result for the star formation history of Carina was previously obtained even by Hurley-Keller et al. (1998). Do they also correspond quantitatively? If we integrate the peak-specific SFR obtained for the LSB over the areas of Carina and Leo I (using directly the size of the LSB remnant would be misleading as this corresponds more to an extended dSph such as Sextans), for a tidal radius of ~ 750 pc (see Mateo 1998), we obtain, for $\alpha = 0.2$, a total SFR between 150 and 350 $M_\odot$ Myr^{-1}, which is rather close to the values of 150–200 $M_\odot$ Myr^{-1} estimated by Hernandéz et al. (2000). Instead, for a higher star formation efficiency, the maximum SFRs are a few factors higher than the observational estimate.

In the case of the HSB satellite, only one much stronger burst occurs after the first pericentric passage, depleting all

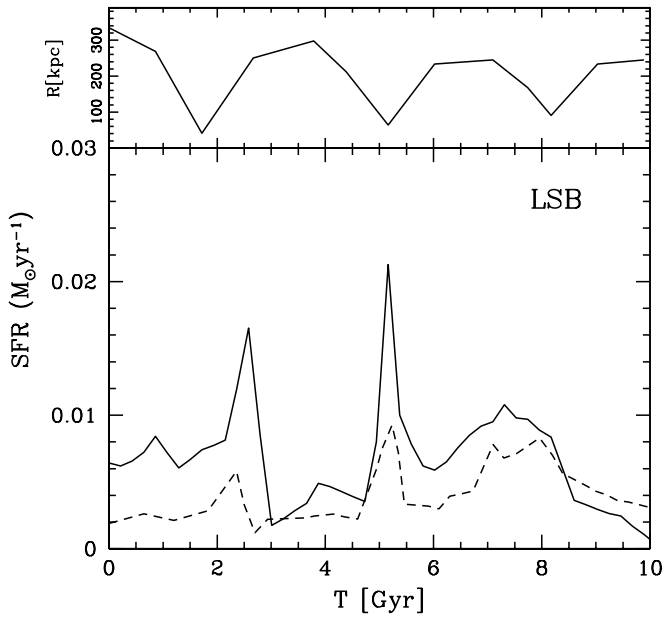

FIG. 31*a*

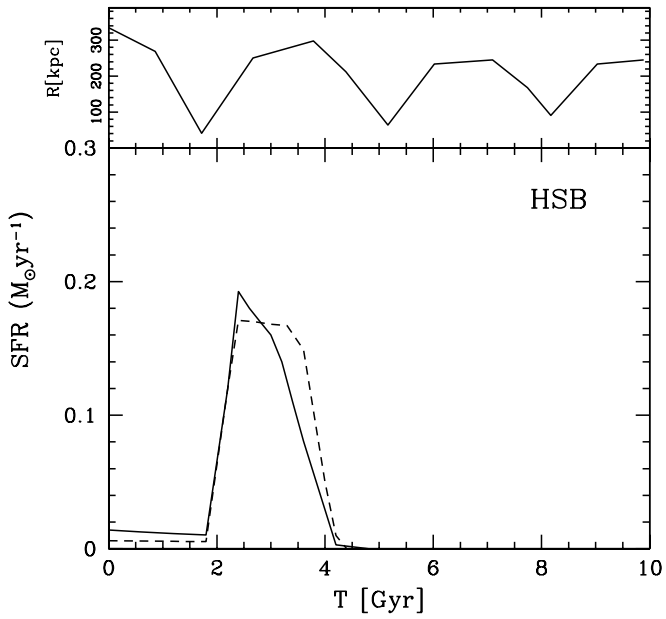

FIG. 31*b*

FIG. 31.—(*a*) Star formation history of the LSB satellite for two values of the efficiency parameter $\alpha = 0.6$ (*solid line*) and $\alpha = 0.2$ (*dashed line*). The specific SFR before first pericentric passage (i.e., before $T = 2$ Gyr) are $\sim 0.00025\ M_\odot\ \mathrm{yr}^{-1}\ \mathrm{kpc}^{-2}$ and $\sim 0.00075\ M_\odot\ \mathrm{yr}^{-1}\ \mathrm{kpc}^{-2}$ for, respectively, $\alpha = 0.2$ and $\alpha = 0.6$, and the total SFR is always calculated integrating over the area of the remnant, which is ~ 4 kpc in radius. (*b*) Star formation history of the HSB satellite for $\alpha = 0.42$ (*solid line*), $\alpha = 0.18$ (*dashed line*). The specific SFR before first pericentric passage is higher than that of the LSB because of the higher surface density of the gas, notwithstanding the lower values of α (these are calibrated in order to obtain the same total SFR of the LSB despite the smaller radius of the HSB). The satellites enter into the Milky Way halo at $T = 0$ and are then followed for 10 Gyr.

the gas in less than ~ 2 Gyr, before the satellite completes the second orbit. Because gas consumption is always extremely fast compared to the orbital time, the results do not depend sensitively on the efficiency parameter α. The maximum star formation rate is almost a factor of 10 higher than in the case of the LSB. This second type of star formation history is present also among observed early-type dwarfs: Draco and Ursa Minor are well-known examples; even the dEs in M31 appear to have had one major episode of star formation (Grebel 1999; Mateo 1998).

Supernovae feedback, which is not included in the derived star formation histories, could have a significant effect, especially in the case of HSBs, given their strong burst. Their star formation rate during the burst is of the order of that measured in the dwarf galaxies analyzed by Martin (1999), which all show strong outflows of gas (even a Local Group dIrr, Sextans A, is included in such a sample sample). Mass-loss rates of about $0.3\ M_\odot\ \mathrm{yr}^{-1}$ are thought to be associated with the prominent Hα shells detected. The velocity of the inflow of gas associated with the bar is of the order of ~ 10 km s^{-1}, while the expanding shell produced by supernovae explosions (which would occur almost instantly compared to the dynamical time of the galaxy) would be moving at up to 100 km s^{-1} (Meurer et al. 1992) and could, in principle, reverse the motion of the gas. However, Mac Low & Ferrara (1999), using a high-resolution Eulerian code to model the ISM in a starbursting dwarf within a massive dark matter halo, have shown that, unless the dwarf has a total mass as low as $10^7\ M_\odot$, the gas mass lost in these outflows is only a few percent of the total mass even for starbursts as intense as $L_\odot \sim 10^{40}$ ergs s^{-1} (a comparable intensity is calculated in the HSB satellite). The holes produced in the gaseous disk recollapse under the influence of the gravity of the galaxy and will settle down again 3–4×10^8 yr after the explosion, again switching on star formation. We can imagine these process repeating several times as new supernovae explosions occur. As a result, the same gas mass will be turned into stars on a longer timescale than in our model. We should still see a first peak of activity, but this will be lower, being soon depressed by the first consistent supernovae explosion, and will be then followed by a less intense, extended activity regulated more by feedback than by the bar inflow. This may well explain why in the dEs, after a first burst, some star formation took place even recently (Grebel 1999). That feedback is important in regulating the star formation of dwarf galaxies has been clearly shown by Ferrara & Tolstoy (2000), who can reproduce the average star formation rates of nearby dIrrs very well. On the other hand, a major drawback of such models, which do not include any environmental influence, is that they cannot reproduce the bursting behavior so commonly observed in nearby dwarfs.

We can ask what the SFR history of the GR 8–like dwarf would be like if we added gas. The disk stellar surface density of GR 8 is pretty close to that of the HSBs, and this would be likely true even for the gaseous disk. Therefore, the specific SFR would be necessarily close to that of HSBs. A clear bar pattern appears after the second pericenter passage and would likely produce a strong burst. The star formation in Draco and Ursa Minor seems to have lasted ~ 3 Gyr according to Hernandéz et al. (2000), and this constraint would be approximately satisfied if we adopt for GR 8 a star formation history similar to that of the HSB. Hernandéz et al. (2000) invoke feedback to explain the abrupt truncation of the star formation for Ursa Minor: in our model this would result automatically from gas consumption. However, the GR 8 model has a mass so low as to fall in the regime of substantial blow-away of the gas by

supernovae according to Mac Low & Ferrara (1999). Adding the effect of supernovae would likely provide a better match to the observations, lowering the amplitude of the burst (see above) while still drastically reducing the star formation later on.

In § 4 we have seen that, while remnants of HSBs have little scatter in their structural properties, remnants of LSBs have a large scatter, being very sensible to the orbital configuration. On orbit with large pericenters, for example, the bar instability is stronger because stripping is less efficient. In this case, a star formation history closer to that of HSBs may result. Therefore, a strong prediction of our model is that dSphs must have a large variety of star formation histories, while dEs should have very similar histories. The data seems to support this conclusion (Grebel 1999; Mateo 1998).

From the final density profiles of the gas (Fig. 14), we can argue that a compact stellar nucleus would form in the remnants of HSBs. A crude conversion of the gas surface density directly into stellar surface density implies that the central surface brightness should be boosted by ~ 2 mag inside a scale of 500 pc, assuming the same $(M/L)_{*B}$ of the preexisting stellar component (this is a conservative choice shortly after the burst has started because the blue luminosity would be higher at that time). Such a central luminosity spike would probably resemble that associated with the blue nucleus in NGC 205 (Ferguson & Binggeli 1994). The fraction of the newly formed stellar population with respect to the total stellar mass would be $\leq 50\%$ in both the LSBs and HSBs, which is similar to the initial gas fraction. This is not surprising because gas and preexisting stars are stripped to the same extent and most of the gas that remains bound is transformed into stars. However, this also means that if the initial gas/stars ratio in the models were greater than 1, as in some dIrrs (e.g., Sag DIG in the Local Group), the satellite could actually form most of its stars during the interaction.

Because of the bar-driven fueling, young stars in the remnant would be located principally in its central part. This is what is observed in many Local Group early-type dwarfs, well-known examples being Fornax, Carina, Sextans, NGC 147 (Grebel 1999), and Sculptor (Hurley-Keller, Mateo, & Grebel 1999). The much stronger bursts in HSB satellites should give rise to a higher metal enrichment compared to that of LSB satellites because the supernovae rate should be higher. As tidal stirring necessarily implies that the remnants of the robust HSBs are more luminous than the remnants of the fragile LSBs, one would expect a correlation between metallicity and luminosity, similar to that observed in the Local Group, where bright dEs are more metal-rich than dSphs (Mateo 1998). On the other end, a higher metallicity spread should be present in dSphs as a consequence of their star formation being more extended in time. Radial metallicity gradients, with the more metal-rich population sitting in the center of the galaxy, as observed in Fornax (Grebel 1999), are also a natural consequence of the model. However, adding the effect of supernovae is fundamental in order to obtain reliable models of the chemical evolution of the dwarfs (Ferrara & Tolstoy 2000).

8. THE FINAL DISTRIBUTION OF COLD GAS

Figure 32 shows the final cumulative profile of the cold gas component in the tidally stirred dwarfs once consumption by star formation is taken into account. Only the results for the LSB are shown as all the gas is consumed in the HSB, notwithstanding the chosen efficiency. The final $M_{\rm gas}/M_{\rm stars}$ in the LSB remnant is less than 0.1 for $\alpha = 0.2$ and less than 0.025 for $\alpha = 0.6$. The limits derived for the LSB remnant for the lower value of α, which yields star formation rates closer to the observed ones (see previous section) are slightly higher than the limits inferred for $M_{\rm H\,I}/L$ in dSphs (Mateo 1998). However, our simulations lack heating sources, such as supernovae, that could have ionized or even blown out some of the remaining gas.

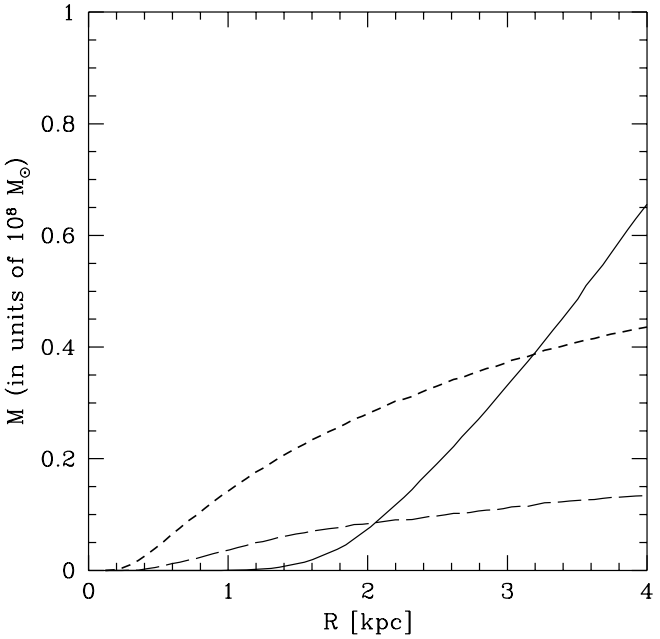

FIG. 32.—Evolution of the cumulative mass profile for the gas in the LSB according to the derived star formation history. We show the results in a region corresponding to the final size of the remnant in run L26. The solid line is used for the initial distribution while the long-dashed and short-dashed lines represent the distribution after 10 Gyr for, respectively, $\alpha = 0.6$ and $\alpha = 0.2$.

The final distribution of the unbound gas yields some interesting predictions. Leading and trailing streams of gas form that parallel the stellar streams. These keep following the satellite's trajectory in the primary potential for the duration of the simulations (more than 7 Gyr). In the case of the LSB satellite, the gaseous streams make up more than 60% of the total initial gas mass. Such extratidal gas is never reaccreted by the dwarf galaxy, contrary to recent claims (Lin & Murray 2000). Particles that end up in the remnant have always been inside the final tidal radius, as was verified by tracing back into time the position of the particles. However, the streams tend to clump at apocenter, where the orbital velocity is low, and chance alignments along the line of sight are possible, as for the stellar streams (§ 5.4). When viewed from within the orbital plane, the streams projected onto the plane of the sky could look like two gas clouds symmetrically distributed around the bound stellar component (Fig. 33). The resulting configuration is very reminiscent of that of the outer H I distribution in Sculptor (Carignan et al. 1998). In addition, similar systemic velocities would be measured for the galaxy and the clouds since these are moving on the same orbit. These results could explain the origin of the outer gas component recently discovered around several Local Group dSphs (Blitz & Robi-

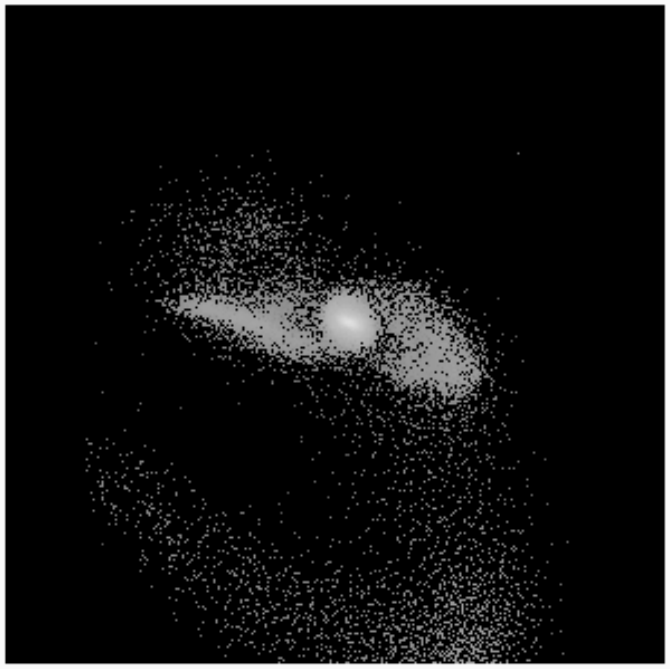

FIG. 33.—Projected distribution of the stripped gas close to apocenter as seen from within the orbital plane in the case of the LSB dwarf (run L26). The color-code logarithmic density is shown (the darker the color, the lower the density). The box is 30 kpc on a side.

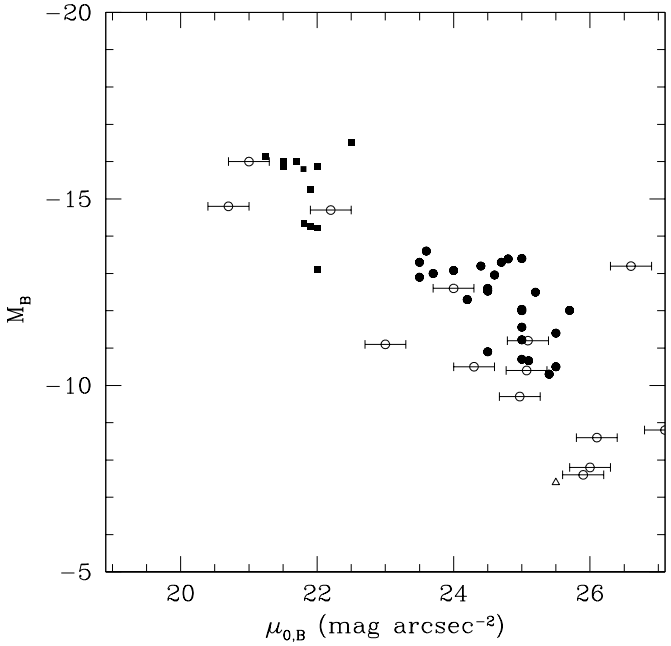

FIG. 35.—The μ-M relation for the remnants in our simulations. Squares are used for remnants of HSBs, filled dots for those of LSBs, and a triangle is used for the remnant of GR 8. B-band absolute magnitudes are measured at the Holmberg radius while $\mu_{0,B}$ is the central surface brightness. Open dots refer to data on real dSphs (belonging to both the Milky Way and M31 subgroups) taken from Mateo (1998); we consider a mean error of 0.3 mag in the determination of their B-band magnitude.

shaw 2000). We note that dEs may be surrounded by only modest amounts of extratidal gas that could easily escape detection because of the considerably reduced effect of tidal stripping in their HSB dIrr progenitors. The same would be true even for dense dwarfs with GR 8–like progenitors, therefore we do not expect prominent gas clouds to be scattered along the orbits of Draco or Ursa Minor. In these cases, our simulations show that rapid consumption within the galaxy is the fate of most of the gas.

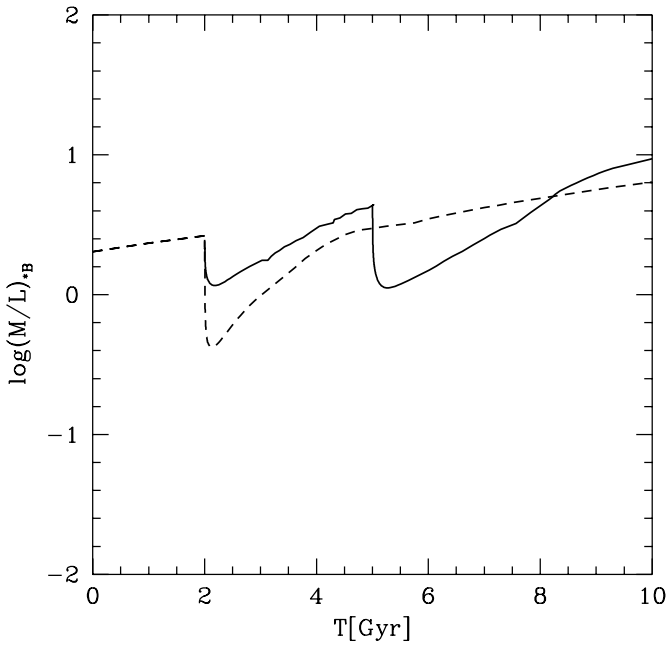

FIG. 34.—Evolution of the B-band stellar mass-to-light ratio as obtained with stellar population synthesis models coupled with the derived star formation histories for the LSB (*solid line*) and for the HSB satellite (*dashed line*). The intensity of the bursts was chosen according to the height of the peaks in the star formation histories, while we used $\tau_{02} = 4 \times 10^8$ yr and $\tau_{03} = 1 \times 10^9$ yr (for the LSB) and $\tau_{02} = 3 \times 10^8$ yr (for the HSB) as time constants (see text, in particular eq. [7]).

9. OBSERVABLE PROPERTIES OF THE REMNANTS

Using stellar population synthesis models (Bruzual & Charlot 1993), we calculated the luminosity and stellar mass-to-light ratios evolution of the remnants according to the derived star formation histories. We employ synthesis models for stellar populations with a metallicity of $\frac{1}{4}$ the solar value. Gerritsen & de Blok (1999) find such low values for the metallicity of LSB galaxies and dSphs in the Local Group have even lower metallicities in their older stellar populations (Mateo 1998). Given a star formation rate $\Psi(t)$, the evolution of the total luminosity L_B of the galaxy in the B band is given by

$$L_B(t) = \int_0^t \Psi(t - \tau) L_B(\tau) d\tau \, , \tag{7}$$

where $L_B(\tau)$ is the luminosity contributed by stars of age τ. We simply assume $\Psi(t) = \Psi_1 + \Psi_2(t) + \Psi_3(t)$, where Ψ_1 is the constant SFR prior to the first pericenter passage, equal to 0.3 $M_\odot$ yr^{-1}, and $\Psi_{2,3}(t) = A \exp(-t/\tau_{02,3})$ represent the bursts ($\Psi_3(t) = 0$ for the HSB). The time and normalization constants of the bursts are derived by naively fitting the star formation histories obtained for the highest value of α (see previous section) in order to evaluate an upper limit for the final luminosity.

In Figure 34, we can see the resulting evolution of the B band stellar mass-to-light ratio, $(M/L)_{*B}$, for both the LSB

and the HSB. The final $(M/L)_{*B}$ are ~ 5 in both cases after 7–8 Gyr (the earlier truncation of the star formation in the HSB is compensated by the much stronger burst) decreasing by more than a factor of 2 with respect to their initial value.

We can now use such information to compute the luminosities of the remnants from $(M/L)_{*B}$ along with their final stellar masses. We consider the value of $(M/L)_{*B}$ reached after 7 Gyr in all cases, which is equal to 5, while for GR 8 we choose $(M/L)_{*B} = 6.5$ because it would be observed at least 10 Gyr after it entered the Milky Way halo (as required by infall at $z \geq 2$). The surface brightness can be obtained as well: the resulting profiles were actually shown in § 5. In § 5.3 we gave lower limits on the final value of M/L. We can now compute more precisely the final M/L by multiplying the obtained $(M/L)_{*B}$ times $M_{\rm dark}/M_{\rm stars}$ (the latter is directly measured in the remnants). The resulting M/L are in the range 6–30, except for the remnant of GR 8, which would have $M/L \geq 70$ ($M_{\rm dark}/M_{\rm stars}$ is ~ 12), well matching the inferred values for Draco and Ursa Minor.

As shown in Mayer et al. (2001), it is possible to construct the fundamental plane for the remnants coupling the information directly provided by the simulations with the model for the photometric evolution described in this section. Such a fundamental plane reproduces very well that of observed early-type dwarfs (Ferguson & Binggeli 1994). Here we show the correlation between luminosity and surface brightness, the μ_B-M_B relation (Fig. 35), which also matches well the observations (Ferguson & Binggeli 1994). The range of surface brightness and luminosity spanned by the remnants of LSBs and HSBs corresponds to that spanned by, respectively, dSphs and dEs (see Mateo 1998).

10. DISCUSSION AND CONCLUSION

We have shown that disklike dwarf galaxies resembling nearby dIrrs can be transformed into dSphs and dEs as a result of 2–3 strong tidal shocks at the pericenters of their orbits within the primary halo. Our model naturally leads to the morphology-density relation observed in the Local Group: present-day LG dIrrs, being close to the boundary of the Local Group zero-velocity surface (van den Bergh 1999), have just decoupled from the Hubble flow and still have to feel the tidal forcing by the dominant galaxies. The transformation results from a combination of mass loss by tidal stripping plus removal of angular momentum and vertical heating caused by tidally induced dynamical instabilities. The different impact of mass stripping and of triggered instabilities in HSB dIrrs versus LSB dIrrs naturally explains the different structural properties of dEs versus dSphs.

The fact that, at least in the Local Group, the number of dEs is lower compared to that of dSphs (only 3 around M31 against nearly 20 dSphs in the whole Local Group) can be understood in terms of the skewness of the number density of disk galaxies toward lower surface brightness, especially at low luminosities (Sprayberry et al. 1997; Bothun, Impey, & McGaugh 1997; O'Neil & Bothun 2000). Photometric surveys of other nearby groups will be useful to ascertain if the relative proportion of dSphs versus dEs is a general trend among faint dwarf satellites. According to our model, this can be explained with a prevalence of objects with shallow halo profiles (namely, LSB dIrrs) among the progenitors of early-type dwarfs. This may have an impact on our understanding of structure formation. In fact, in CDM cosmogonies, the average central density of halos on the mass scale of dwarfs is higher than that of our LSB models (the GR 8 model being an exception), the latter being closer to the typical central density of small halos in WDM models (Bode et al. 2001; Eke et al. 2001).

On the other end, the origin of the few extremely dark matter dominated dSphs, Draco and Ursa Minor, is well explained assuming a CDM scenario. In fact, in the latter model, one expects that the dwarf satellites forming at high redshift have a typical central dark matter density as high as that of the faint dIrr GR8. These small galaxies are very robust to tides, but if they infall at $z \geq 2$, their orbital times are likely so small that they can double the number of pericenter passages relative to the satellites infalling at $z \leq 1$. By $z = 0$, they transmute into tiny spheroidal galaxies but maintain very high dark matter contents, just like Draco and Ursa Minor. However, one can actually use such high-density dwarfs to place a lower limit on the mass of the dark matter particles in WDM models (Dalcanton & Hogan 2001).

In this paper, we have shown that tidal stirring is effective if satellites have sufficiently low orbital times, notwithstanding the moderate eccentricities of their orbits. LSB satellites on circular orbits very close to the Milky Way can even disrupt because of their large, low-density disks and will produce long-lasting density enhancements that resemble the dwarf spheroidal Sagittarius. However, the farthest dSphs, Leo I and Leo II, must be moving on fairly eccentric orbits (apo/peri > 3) in order to be transformed. These distant dwarfs place also a constraint on the structure of the primary halo, which must be as large and massive as expected in cold dark matter models for them to have sufficiently small orbital times.

Our evolutionary mechanism is able to explain the difference in gas content between dwarf spheroidals and dwarf irregulars as well as the recent observations of extratidal gas around some Local Group dSphs. In addition, we obtained both periodic star formation histories and single-burst star formation histories for, respectively, LSB and HSB satellites, reproducing the variety observed among Local Group early-type dwarfs. With tidal stirring operating in a hierarchical structure formation scenario, we expect dSphs closer to the primary galaxies to have stars typically older then those in more distant ones because they should have, on average, an earlier infall time (see § 5.3) and thus an earlier bursting phase. Van den Bergh (1994) has pointed out that there are indications of such a correlation among Local Group dSphs.

The stars stripped in both the HSB and LSB are prevalently those making up the oldest component (with age greater than 7 Gyr), as we know that the new star formation takes place in the inner, bound regions of the satellite. As a result, we expect the outer stellar halo of the Milky Way to be abundant in old, low-metallicity stars. If, as suggested by the results of the LSB runs, we assume that Carina, Fornax, Leo I, Leo II, Sculptor, Sextans, and Sagittarius have typically lost $\sim 60\%$ of their original stellar mass, we find out that dwarf spheroidals should have contributed at least 10^9 solar masses to the old stellar halo. These should be still recognizable as part of distinct streams tracing the orbits of the satellites, with a maximum surface brightness (at the turning points of the orbits) of just 30 mag arcsec^{-2} (B band). Spectroscopic evidence for stellar streams from the dSph Carina has been claimed (Majewski et al. 2000) and

the northern stream of Sagittarius or a new stream associated to another disrupted nearby dwarf has recently been observed (Martinéz-Delgado et al. 2001). Future astrometric missions, such as the *Space Interferometry Mission* (*SIM*) and *Global Astrometric Interferometer for Astrophysics* (*GAIA*) (Gilmore et al. 1998; Helmi et al. 1999; Helmi & de Zeeuw 2000), should reveal such faint features and will also carry out high-quality measurements of proper motions for many satellites of the Milky Way, thus providing a test for the orbital configurations used in this model.

Stellar streams projecting close to the line of sight can produce subtle observational effects for fragile LSB satellites, thereby inflating the measured velocity dispersions. Their signature should be an apparent rotation of the dwarf and could have been observed in Ursa Minor (Hargreaves et al. 1994a). Instead, velocity dispersion anisotropy cannot inflate significantly the measures of the mass-to-light ratios.

Van den Bergh (2000) and Grebel (1999) have noted recently that some peripheral globular clusters in Local Group dSphs (e.g., Fornax) are younger (less than 10 Gyr) than globular clusters in the outer halo of the Galaxy. In our scenario, they could have formed in the strongest phase of the tidal shock, immediately following pericenter passage, but in this case we would expect to find them quite close to the center. Subsequently, dynamical friction can only take them even closer to the center, apparently leading to a conflict with observations. However, Oh, Lin, & Richer (2000) have found that tidal mass loss provoked by the primary galaxy would cause a diffusion of the clusters' orbits toward the outer regions as they preserve their radial and azimuthal actions during the gradual decline of the dwarf's potential. Therefore, we can argue that tidal stirring provides a mechanism for the formation of globular clusters in dSphs and, at the same time, can explain their spatial distribution.

From the evolution of the stellar mass-to-light ratio, it turns out that HSB satellites have $(M/L)_{*B}$ as low as 0.4 during the bursting phase. The high blue luminosity would come from the central part of the galaxies, which could resemble the blue compact dwarfs (BCDs) observed by Guzmán et al. (1997) at intermediate redshift ($z \sim 0.5$–0.7). The velocity widths of these galaxies correspond to those of the largest among our HSB satellites (between 50 and 75 km s^{-1}) and the total blue luminosities would also be comparable (model HM1 reaches a luminosity of about $M_B = -20$ in this phase). Interestingly, Guzmán et al. (1997) conclude that fading would transform BCDs into objects similar to NGC 205 and the other dEs after several gigayears while none of them could fade so much as to resemble dSphs. The latter conclusion coincides with our claim that HSB dIrrs are the progenitors of dEs and not of the fainter dSphs. Future investigations aimed at searching for massive galaxies in the vicinity of blue compact dwarfs may shed light on the connection with tidally stirred dwarfs.

The authors thank G. Gavazzi, C. Gallart, M. Vietri, R. Bower, A. Helmi, and S. Ghigna for stimulating discussions and the referee Mario Mateo for many useful comments that improved the paper. Simulations were carried out at the CINECA (Bologna) and ARSC (Fairbanks) supercomputing centers.

REFERENCES

Abadi, M. G., Moore, B., & Bower, R. G. 1999, MNRAS, 308, 947
Armandroff, T. E., Olszewski, E. W., & Pryor, C. 1995, AJ, 110, 2131
Athanassoula, E., & Sellwood, J. A. 1986, MNRAS, 221, 213
Babul, A., & Rees, M. 1992, MNRAS, 255, 346
Barnes, J. 1988, ApJ, 331, 699
Bender, R., Burstein D., & Faber, S. M. 1992, ApJ, 399, 462
Bender, R., & Nieto, J. L. 1990, A&A, 239, 97
Bica, E., Alloin, D., & Schmidt, A. A. 1990, A&A, 228, 23
Binggeli, B., & Cameron, L. M. 1991, A&A, 252, 27
Binney, J., & Tremaine, S. 1987, Galactic Dynamics (Princeton Univ. Press)
Blitz, L., & Robishaw, T. 2000, ApJ, 541, 675
Blitz, L., Spergel, D. N., Teuben, P., Hartmann, D., & Burton, W. B. 1999, ApJ, 514, 818
Bode, P., Ostriker, J., & Turok, N. 2001, ApJ, 556, 93
Bothun, G. D., Impey, C., & McGaugh, S. 1997, PASP, 109, 745
Bottema, R. 1997, A&A, 328, 517
Bruzual, G., & Charlot, S. 1993, ApJ, 405, 538
Bullock, J. S., Kolatt, T. S., Sigad, Y., Somerville, R. S., Kravtsov, A. V., Klypin, A. A., Primack, J. R., & Dekel, A. 2001, MNRAS, 321, 559
Bullock, J. S., Kravtsov, A. V., & Weinberg, D. H. 2000, ApJ, 539, 517
Burkert, A., & Silk, J. 1997, ApJ, 488, L55
Carignan, C., Beaulieu, S., Côté, S., Demers, S., & Mateo, M. 1998, AJ, 116, 1690
Carignan, C., Beaulieu, S., & Freeman, K. C. 1990, AJ, 99, 178
Carter, D., & Sadler, E. M. 1990, MNRAS, 245, P12
Colpi, M., Mayer, L., & Governato, F. 1999, ApJ, 525, 720
Cote, S., Freeman, K. C., & Carignan C. 1997, in ASP Conf. Ser. 117, Dark and Visible Matter in Galaxies, ed. M. Persic & P. Salucci (San Francisco: ASP), 52
Cote, S., Mateo, M., Olszewski, E. W., & Cook, K. H. 1999, ApJ, 526, 147
Dalcanton, J. F., & Hogan, C. J. 2001, ApJ, in press
de Blok, W. J. G., & McGaugh, S. S. 1997, MNRAS, 290, 533
de Grijs, R., Peletier, R. F., & Van der Kruit P. C. 1997, A&A, 327, 966
Dekel, A., & Silk, J. 1986, ApJ, 303, 39
Dikaiakos, M., & Stadel, J. 1996, Conf. Proc. of the International Conference on Supercomputing (New York: Assoc. for Computing Machinery)
Dohm-Palmer, R. C., et al. 1997, AJ, 114, 2527
———. 1998, AJ, 116, 1227
Efstathiou, G. 1992, MNRAS, 256, P43
Einasto, J., Saar, E., Kaasik, A., & Chernin, A. D. 1974, Nature, 252, 111
Eke, V. R., Cole, S., & Frenk, C. S. 1996, MNRAS, 282, 263
Eke, V. R., Navarro, J. F., & Steinmetz, M. 2001, ApJ, 554, 114
Evans, N. W., & Kerins, E. 2000, ApJ, 529, 917
Faber, S. M., & Lin, D. N. C. 1983, ApJ, 266, L17
Ferguson, H. C., & Binggeli, B. 1994, A&A Rev., 6, 67
Ferguson, H. C., & Sandage, A. 1991, AJ, 101, 765
Ferrara, A., & Tolstoy, E. 2000, MNRAS, 313, 291
Franx, M., Illingworth, G., & de Zeeuw, T. 1991, ApJ, 383, 112
Friedli, D. 1999, in ASP Conf. Ser. 187, The Evolution of Galaxies on Cosmological Timescales, ed. J. E. Beckman & T. J. Mahoney (San Francisco: ASP)
Friedli, D., & Benz, W. 1993, A&A, 268, 65
Fux, R., Martinet, L., & Pfenninger, D. 1995, in IAU Symp. 169, Unsolved Problems of the Milky Way, ed . L. Blitz & P. Teuben (Dordrecht: Kluwer), 125
Gallart, C., et al. 1999, ApJ, 514, 665
Gallart, C., Martinez-Delgado, D., Gomez-Flechoso, M. A., & Mateo, M. 2001, AJ, 121, 2572
Gelato, S., & Sommer-Larsen, J. 1999, MNRS, 303, 321
Gerritsen, J. P. E., & de Blok, W. J. G. 1999, A&A, 342, 655
Ghigna, S., Moore, B., Governato, F., Lake, G., Quinn, T., & Stadel J. 1998, MNRAS, 300, 146
Gilmore, G. F., et al. 1998, Proc. SPIE, 3350, 541
Gnedin, O. Y., Hernquist, L. & Ostriker, J. 1999, ApJ, 514, 109
Gnedin, O. Y., & Ostriker, J. 1999, ApJ, 513, 626
Grebel, E. K. 1999, in IAU Symp. 192, The Stellar Content of Local Group Galaxies, ed. P. Whitelock & R. Cannon (San Francisco: ASP), 17
Gunn, J. E., & Gott, J. R. 1972, ApJ, 176, 1
Guzmán, R., et al. 1997, ApJ, 489, 559
Hargreaves, J. C., Gilmore, G., & Annan, J. D. 1996, MNRAS, 279, 108
Hargreaves, J. C., Gilmore, G., Irwin, M. J., & Carter, D. 1994a, MNRAS, 269, 957
———. 1994b, MNRAS, 271, 693
Held, E. V., Mould, J. R., & de Zeeuw, P. T. 1990, AJ, 100, 415
Held, E. V., de Zeeuw, P. T., Mould, J. & Picard, A. 1992, AJ, 103, 851
Heller, C. H., & Shlosman, I. 1994, ApJ, 424, 84
Helmi, A., & de Zeeuw, T. 2000, MNRAS, 323, 529
Helmi, A., White, S. D. M., de Zeeuw, P., & Zhao, H. 1999, Nature, 402, 53
Hernandéz, X., Gilmore, G., & Valls-Gabaud, D. 2000, MNRAS, 317, 831
Hernquist, L. 1993, ApJS, 86, 389
Hernquist, L., & Katz, N. 1989, ApJS, 70, 419
Hernquist, L., & Weinberg, M. D. 1989, MNRAS, 238, 407

Hodge, P. W. 1971, ARA&A, 9, 35
Hodge, P. W., Smith, T. R., Eskridge, P. B., MacGillivray, H. T., & Beard, S. M. 1991a, ApJ, 369, 372
———. 1991b, ApJ, 379, 621
Hoffman, G. L., Salpeter, E. E., Farhat, B., Roos, T., Williams, H., & Helou, G. 1996, ApJS, 105, 269
Hurley-Keller, D., Mateo, M., & Grebel, E. K. 1999, ApJ, 523, L25
Hurley-Keller, D., Mateo, M., & Nemec, J. 1998, AJ, 115, 1840
Ibata, R. A., & Lewis, G. F. 1998, ApJ, 500, 575
Irwin, M., & Hatzidimitriou, D. 1995, MNRAS, 277, 1354
James P. 1991, MNRAS, 250, 544
Jobin, M., & Carignan, C. 1990, AJ, 100, 648
Jones, D. H., et al. 1996, ApJ, 466, 742
Kalberla, P. M. W., & Kerp, J. 1998, A&A, 339, 745
Karachentsev, I. D., et al. 2000, A&A, 363, 117
Kennicutt, R. C., Jr. 1998, ApJ, 498, 541
Kent, S. M. 1987, AJ, 94, 306
Klessen, R., & Kroupa, R. 1998, ApJ, 498, 143
Klypin, A., Kravtsov, A. V., Valenzuela, O., & Prada, F. 1999, ApJ, 522, 82
Knebe, A., Kravtsov, A. V., Gottlober, S., & Klypin, A. 2000, MNRAS, 317, 630
Kravtsov, A. V., & Klypin, A. A. 1999, ApJ, 520, 437
Kroupa, P. 1997, NewA, 2, 139
Kroupa, P., & Bastian, U. 1997, NewA, 2, 139
Kuhn, J. R. 1993, ApJ, 409, L13
Kuhn, J. R., & Miller, R. H. 1989, ApJ, 341, L41
Lacey, C., & Cole, S. 1993, MNRAS, 262, 627
———. 1994, MNRAS, 271, 676
Lake, G. 1990, MNRAS, 244, 701
Lin, D. N. C., & Murray, S. D. 2000, in Dwarf Galaxies and Cosmology, ed. T. X. Thuân, C. Balkowski, V. Cayatte, & J. Trâm Thanh Van (Paris: Editions Frontières)
Little, B., & Tremaine, S. 1987, ApJ, 320, 493
Lo, K. Y., Sargent, W. L. W., & Young, K. 1993, AJ, 106, 507
Mac Low, M. M., & Ferrara, A. 1999, ApJ, 513, 142
Majewski, S. R., Ostheimer, J. C., Patterson, R. J., Kunkel, W. E., Johnston, K. V., & Geisler, D. 2000, AJ, 119, 760
Martin, C. L. 1999, ApJ, 513, 156
Martinez-Delgado, D., Aparicio, A., Gómez-Flechoso, M. Á., Carrera, R. 2001, ApJ, 549, L199
Mateo, M. 1998, ARA&A, 36, 435
Mayer, L., Governato, F., Colpi, M., Moore, B., Quinn, T., Wadsley, J., & Stadel, J. 2001, ApJ, 547, L123
Merritt, D. & Sellwood, J. A. 1994, ApJ, 425, 551
Meurer, G. R., Freeman, K. C., Dopita, M. A., & Cacciari, C. 1992, AJ, 103, 60
Mihos, J. C., McGaugh, S., & de Blok, W. J. G. 1997, ApJ, 477, L79
Miwa, T., & Noguchi, M. 1998, ApJ, 499, 149
Mo, H. J., Mao, S., & White, S. D. M. 1998, MNRAS, 296, 847
Moore, B., Ghigna, S., Governato, F., Lake, G., Quinn, T., Stadel, J., & Tozzi, P. 1999b, ApJ, 524, L19
Moore, B., Katz, N., & Lake, G. 1996a, ApJ, 457, 455
Moore, B., Katz, N., Lake, G., Dressler, A., & Oemler, A., Jr. 1996b, Nature, 379, 613
Moore, B., Lake, G., & Katz, N. 1998, ApJ, 495, 139
Moore, B., Lake, G., Quinn, T., & Stadel, J. 1999a, MNRAS, 304, 465
Murali, C. 2000, ApJ, 529, L81
Navarro, J. F., Eke, V. R., & Frenk, C. S. 1996, MNRAS, 283, L72
Oh, K. S., Lin, D. N. C., & Richer, H. B. 2000, ApJ, 531, 727
O'Neil, K., & Bothun, G. 2000, ApJ, 529, 811
Peebles, P. J. E., Melott, A. L., Holmes, M. R., & Jiang, L. R. 1989, ApJ, 345, 108
Persic, M., & Salucci, P. 1997, in ASP Conf. Ser. 117, Dark and Visible Matter in Galaxies, ed. M. Persic & P. Salucci (San Francisco: ASP), 1
Piatek, S., & Pryor, C. 1995, AJ, 109, 1071
Pryor, C. 1994, in Proc. ESO/OHP Workshop on Dwarf Galaxies, ed. G. Meylan & P. Prugniel (Garching: ESO), 323
Quilis, V., Moore, B., & Bower, R. 2000, Science, 288, 1617
Quinn, T., Katz, N., & Efstathiou, G. 1996, MNRAS, 278, 49
Raha, N., Sellwood, J. A., James, R. A., & Kahn, F. D. 1991, Nature, 352, 411
Rosati, P., Borgani, S., della Ceca, R., Stanford, A., Eisenhardt, P., & Lidman, C. 2001, in Large Scale Structure in the X-ray Universe, ed. M. Plionis & I. Georgantopoulos (Paris: Atlantisciences), 13
Schweitzer, A. E., Cudworth, K. M., Majewski, S. R., & Suntzeff, N. B. 1995, AJ, 110, 2747
Sofue, Y. 1999, PASJ, 51, 445
Sprayberry, D., Impey, C. D., Irwin, M. J., & Bothun, G. D. 1997, ApJ, 482, 104
Springel, V., & White, S. D. M. 1999, MNRAS, 307, 162
Steinmetz, M., & White, S. D. M. 1997, MNRAS, 288, 545
Toomre, A., & Toomre, J. 1972, ApJ, 178, 623
van den Bergh, S. 1994, AJ, 107, 1328
———. 1996, PASP, 108, 986
———. 1999, A&A Rev., 9, 273
———. 2000, ApJ, 530, 777
Van der Kruit, P. C., & de Grijs, R. 1999, A&A, 352, 129
Weinberg, M. D. 1994a, AJ, 108, 1398
———. 1994b, AJ, 108, 1403
———. 1994c, AJ, 108, 1414
———. 2000, ApJ, 532, 922
White, S. D. M., & Frenk, C. S. 1991, ApJ, 379, 52
White, S. D. M., & Rees, M. J. 1978, MNRAS, 183, 341
Wilkinson, M. I., & Evans, N. W. 1999, MNRAS, 310, 645
Young, L. M., & Lo, K. Y. 1997, ApJ, 476, 127
Zaritsky, D., Smith, R., Frenk, C. S., & White, S. D. M. 1993, ApJ, 405, 464
Zwaan, M. A., van der Hulst, J. M., de Blok, W. J. G., & McGaugh, S. S. 1995, MNRAS, 273, L35